Materials Advances

ROYAL SOCIETY OF CHEMISTRY

PAPER

View Article Online
View Journal | View Issue

Cite this: *Mater. Adv.*, 2026, 7, 4307

Computational evaluation of pressure effects on cubic ferromagnetic perovskites $ACrBr_3$ (A = K, Rb, Cs, Fr): materials engineering perspectives for spintronics and optoelectronics *via* DFT

Basanti Banik,[a] Mst. Shamima Khanom,[a] Md. Rony Hossain *[ab] and Farid Ahmed[a]

In this study, the pressure-dependent properties of cubic ferromagnetic metal halide single perovskites $ACrBr_3$ (A = K, Rb, Cs, Fr) were systematically investigated using density functional theory (DFT). The tolerance factor and octahedral factor indicate that the investigated compounds are stable in a cubic structure having the $Pm\bar{3}m$(221) space group. Structural analysis shows that both unit cell volume and lattice constants decrease with the increasing external hydrostatic pressure range (0–30 GPa). Mechanical stability is confirmed through Born stability criteria, and pressure enhances the elastic constants, further supporting their robustness for device integration. Spin-polarized band structure and density of states (DOS) analyses confirm the half-metallicity, where the spin-up state is metallic and the spin-down state exhibits a band gap. Our studied materials have 100% spin polarization at the Fermi level. Pressure decreases the band gap for all of our investigated materials. The total magnetic moment in all compounds remains approximately an integer value, confirming their suitability for spintronic applications. Thermodynamic parameters, including Debye temperature and melting temperature, exhibit an upward trend with increasing pressure, indicating enhanced stability. Optical properties such as dielectric constants, conductivity, absorption coefficient, reflectivity, refractive index, and loss functions of our studied materials show the highest intensity in the UV region and increase with the applied pressures. These findings highlight the multifunctional potential of $ACrBr_3$ (A = K, Rb, Cs, Fr) perovskites in next-generation spintronic and optoelectronic devices.

Received 8th February 2026,
Accepted 13th March 2026

DOI: 10.1039/d6ma00182c

rsc.li/materials-advances

1. Introduction

Spintronics has emerged as an important research domain in modern condensed-matter and device physics, as it offers an alternative pathway to conventional charge-based electronics by utilizing electron spin.[1,2] Recently, it has been found that half metals, a novel class of materials, are intriguing options in the area of spintronics. A half-metallic material exhibits metallic characteristics for one spin state while displaying semiconductor or insulator behavior for the opposite spin state. Therefore, we can classify these materials as hybrid materials due to the distinct electronic properties associated with the two spin states. Spin-polarized currents eliminate thermal challenges that integrated circuits and other electronic equipment frequently face, since they do not lose energy as heat.[3] NiMnSb and PtMnSb half-Heusler materials are the first half-metallic ferromagnets discovered by Groot *et al.*[4] Afterwards, diverse structures of various half-metallic ferromagnetic materials were investigated, such as spinels $MgNiX_4$,[5] single perovskites $PrMnO_3$[6] and $BaNpO_3$,[7] double perovskites Cs_2AgMBr_6[8] and Ba_2XNbO_6,[9] Cr doped TiO_2,[10] half-Heusler alloy CoTcSn,[11] ternary half-Heusler alloy GeNaZ,[12] full-Heusler alloy CoNiMnSi,[13] and zinc blende CrSb.[14] Transition metal-based cubic perovskites show remarkable half-metallic ferromagnetic properties.

The typical formula for perovskite materials is ABX_3, where A and B are cations, while X is an oxygen or a halogen. The A site is occupied by an alkali or alkaline-earth metal, whereas the B site is typically filled by transition-metal or f-block elements.[15] Due to their novel chemical formulations, crystal structures, and excellent magnetic and optoelectronic features, metal halide perovskites (MHPs) have recently gained a lot of attention and have been considered for various uses, including photovoltaics, photonics, light-emitting diodes, and light-controlling magnetic devices and photonics.[16–19] Lead-based perovskites are disadvantageous for massive applications due to toxicity and instability in the presence of heat, light, and moisture, although they have potential uses.[20] As a result, materials based on lead-free

[a] *Department of Physics, Jahangirnagar University, Savar, Dhaka, 1342, Bangladesh. E-mail: rony.hossainb@gmail.com*
[b] *Department of Software Engineering, Daffodil International University, DSC, Birulia, Savar, Dhaka-1216, Bangladesh*

perovskites such as A_2BBiCl_6[21] and X_2YBiCl_6[22] have become particularly desirable.

Materials' properties can be tailored through the application of various external control parameters, enabling systematic modulation of their functional behavior.[23] Researchers have been showing particular interest in the pressure effect on halide perovskites[24,25] as the influence of pressure on the structural, optical, mechanical, and electrical characteristics of materials is significant. Higher applied pressure compresses the crystal lattice and shrinks the unit-cell volume, which causes the electronic band gap to become smaller, as observed in various papers.[26] It is possible to change the band gap from indirect to direct under hydrostatic pressure.[27]

One of the most effective methods for accurately conducting theoretical research on the physical and chemical properties of a significant number of condensed matter systems is *via* the application of first principles studies.[28] The present study provides a theoretical investigation of transition-metal-based halide single perovskites $ACrBr_3$ (A = K, Rb, Cs, Fr) over the pressure range of 0–30 GPa (0, 10, 20, and 30 GPa) for potential applications in optoelectronics and spintronics.

Our results match those previously published by Alburaih *et al.* for $KCrBr_3$[29] and Ullah *et al.* for $RbCrBr_3$[30] at 0 GPa. This similarity indicates that the computational method used in this work is reliable, confirming the validity of our present study. What makes our research unique is that it looks at how pressure affects the different properties of our materials for possible applications in multiple fields. B-site elements dominate the electronic behavior, as the compound retains its half-metallicity regardless of whether the A-site is occupied by K, Rb, Cs, or Fr.

2. Computational details

We utilized density functional theory (DFT) based first-principles methods implemented in the Cambridge Serial Total Energy Package (CASTEP), where the plane-wave pseudopotential approach was applied for all calculations.[31] OTFG ultrasoft pseudopotentials were employed for addressing the charged particle interactions.[32] Geometry optimization was performed with convergence criteria: an energy tolerance of 2×10^{-5} eV per atom, a maximum force of 0.05 eV $Å^{-1}$, a maximum stress of 0.1 GPa, a maximum displacement of 0.002 Å, and maximum iterations of 1000 using the BFGS (Broyden–Fletcher–Goldfarb–Shanno) algorithm.[33] The Monkhorst–Pack scheme was utilized for sampling *k*-points in the Brillouin zone. We used a 400 eV plane-wave cutoff and a $4 \times 4 \times 4$ *k*-point mesh for all of our calculations throughout our investigations. For evaluating exchange–correlation energy, the spin-polarized GGA functional was implemented using the Perdew–Berke–Ernzerhof (PBE) approach for structural, electrical, magnetic, and optical properties.[34,35] To obtain more accurate electronic and magnetic results, we use the GGA+*U* approximation, which introduces a Hubbard *U* term to account for the localized Coulomb interactions among strongly correlated electrons. Elastic and thermal properties were calculated using the GGA-PBEsol functional for refined reliability.[36]

3. Results and discussion

3.1 Structural features

Our investigated $ACrBr_3$ (A = K, Rb, Cs, Fr) materials are all transition metal-based cubic perovskites having a space group $Pm\bar{3}m$ (international number 221) and 5 atoms in the formula unit, in which A site atoms are positioned at K/Rb/Cs/Fr at (0,0,0), Cr is at $\left(\frac{1}{2},\frac{1}{2},\frac{1}{2}\right)$ and Br is at $\left(0,\frac{1}{2},\frac{1}{2}\right)$ Wyckoff atomic Positions. The polyhedral view of our studied compounds is shown in Fig. 1(a). Convergence tests were performed using $4 \times 4 \times 4$, $6 \times 6 \times 6$, and $8 \times 8 \times 8$ *k*-point meshes and cutoff energies from 300 to 600 eV, as shown in Fig. 1(b). Since the energy change was very small, and the lowest energy was obtained at $4 \times 4 \times 4$, a cutoff energy of 400 eV with a $4 \times 4 \times 4$ *k*-point mesh was used for all calculations. Table 1 demonstrates the lattice parameters, unit cell volume, and energy both under spin-polarized and non-spin-polarized conditions using the GGA functional at 0, 10, 20, and 30 GPa pressures (Table 2).

All four examined perovskites reveal a ferromagnetic state with the lowest energy, which makes it energetically more favorable than both the antiferromagnetic and non-magnetic states shown in Table 1. The apparent rise in cell volume from the non-magnetic to magnetic condition represents a magnetoelastic effect that influences the material's structural characteristics.[15] Pressure decreases the lattice constants and lattice volume, as seen from Table 1 and Fig. 2(a) and (b). Normalized lattice parameters and normalized volume are also presented in Fig. 2(d) and (e) to better understand the pressure effect among them. Any deviance from the optimal cubic structure can be assessed by the tolerance factor (t) that typically ranges from 0.81 to 1.11 for cubic perovskites.[37] The Goldschmidt tolerance factor, t, is given as,

$$t = 0.707\frac{r_A + r_{Br}}{\{r_{Br} + r_{Cr}\}} \quad (1)$$

where r_A, r_{Br}, and r_{Cr} represent the atomic radii of the A-site atom, Br atom, and Cr atom, respectively, which are calculated by using Shannon's effective ionic radii, and the values of t are depicted in Table 3. These values are close to unity, suggesting that the compounds are geometrically compatible with the cubic perovskite structure, although slight deviations may indicate minor structural distortions. In addition, the octahedral factor is determined using the following formula,[2] and Table 3 shows that its values fall within the expected range.

$$\mu = \frac{r_{Cr}}{r_{Br}} \quad (2)$$

The formation energies of $ACrBr_3$ are calculated to make sure that they might be fabricated experimentally using the following expression,[38]

$$E_{Formation}(ACrBr_3) = \frac{\left[E(ACrBr_3) - E_A^{Bulk} - E_{Cr}^{Bulk} - 3E_{Br}^{Bulk}\right]}{n} \quad (3)$$

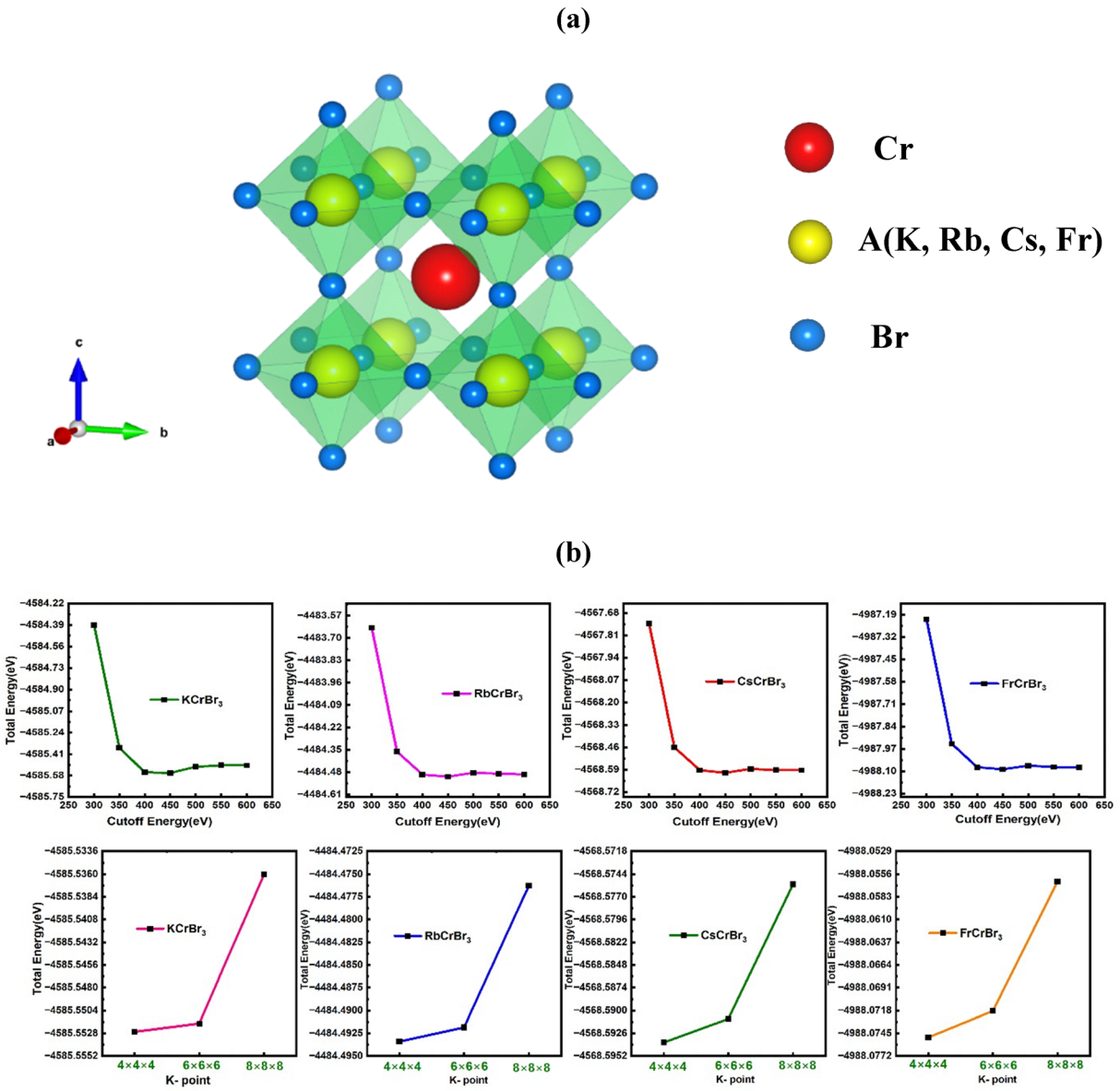

Fig. 1 (a) Polyhedral view of the unit cell and (b) cutoff energy, k-point convergence test of the $ACrBr_3$ (A = K, Rb, Cs, Fr) perovskites.

$$E_{\text{Formation}}(ACrBr_3; P) = \frac{[E(ACrBr_3; P) - E(A; P) - E(Cr; P) - 3E(Br; P)]}{n} \quad (4)$$

Here $E(ACrBr_3)$ denotes the total energy of our compound and E_A^{Bulk}, E_{Cr}^{Bulk}, and E_{Br}^{Bulk} represent the total atomic energies of A, Cr, and Br atoms under bulk conditions, which are determined from the structural optimization calculations. The determined negative values of formation energies for all of our compounds ensure synthesizability and that our materials are energetically favorable relative to their isolated constituent elements.[39] The expression for cohesive energy is given as:[12]

$$E_{\text{Cohesive}}^{(ACrBr_3)} = \left(E_{\text{iso}}^{A} + E_{\text{iso}}^{Cr} + 3E_{\text{iso}}^{Br}\right) - E_{\text{Total}}^{ACrBr_3} \quad (5)$$

Here, E_{iso}^{A}, E_{iso}^{Cr} and E_{iso}^{Br} represent the isolated energies of atom A, Cr, and Br, respectively, and $E_{\text{Total}}^{ACrBr_3}$ is the total energy of $ACrBr_3$ calculated from the structural optimization. Our calculated cohesive energy ranges from 10.53 to 12.84 eV. Such large values ensure the chemical stability of our investigated compound. The calculated Mulliken charges, bond lengths, and bond populations of $ACrBr_3$ (A = K, Rb, Cs, Fr) from the GGA method are presented in Table 3 and Fig. 3, 4.

3.2 Elastic and mechanical characteristics

In materials science, elastic constants are vital factors in determining if a crystal structure is mechanically stable, along with knowing other crucial mechanical properties involving brittleness, ductility, stiffness, and anisotropy. The elastic energy

Table 1 Optimized lattice constants a (Å), equilibrium volume V_0 (Å^3), energy, E_{FM} (eV), energy, E_{AFM} (eV), energy E_{NM} (eV) and normalized lattice parameters calculated using the GGA functional at 0, 10, 20 and 30 GPa pressures of $ACrBr_3$ (A = K, Rb, Cs, Fr) compounds

Compounds	Parameters	0 GPa	10 GPa	20 GPa	30 GPa
$KCrBr_3$	Lattice constant a (Å)	5.31	4.94	4.76	4.63
	Non-spin polarized (Å)	5.17, 5.18[29]	4.86	4.68	4.56
	Cell volume, V_0 (FM) (Å^3)	149.52	120.37	107.80	99.24
	Cell volume, V_0 (NM) (Å^3)	138.45	115.13	102.41	94.74
	Energy, E_{FM} (eV)	−4586.98	−4586.34	−4585.24	−4583.94
	Energy, E_{AFM} (eV)	−4586.95	−4586.33	−4585.19	−4583.87
	Energy, E_{NM} (eV)	−4584.60	−4584.27	−4583.15	−4581.97
	Normalized lattice constants a/a_0	1	0.93	0.90	0.87
	Normalized volume V/V_0	1	0.81	0.72	0.66
$RbCrBr_3$	Lattice constant a (Å)	5.34	4.96	4.78	4.65
	Non-spin polarized $a/b/c$ (Å)	5.21, 5.17[30]	4.89	4.70	4.58
	Cell volume, V_0 (FM) (Å^3)	152.52, 138.55[30]	122.38	109.19	100.74
	Cell volume, V_0 (NM) (Å^3)	141.56	116.58	103.99	96.26
	Energy, E_{FM} (eV)	−4486.19	−4485.51	−4484.34	−4483.04
	Energy, E_{AFM} (eV)	−4486.17	−4485.48	−4484.29	−4482.98
	Energy, E_{NM} (eV)	−4483.79	−4483.38	−4482.25	−4481.06
	Normalized lattice constants a/a_0	1	0.93	0.90	0.87
	Normalized volume V/V_0	1	0.80	0.72	0.66
$CsCrBr_3$	Lattice constant a (Å)	5.40	5.01	4.82	4.70
	Non-spin polarized $a/b/c$ (Å)	5.28	4.94	4.75	4.63
	Cell volume, V_0 (FM) (Å^3)	157.57	126.02	112.45	103.80
	Cell volume, V_0 (NM) (Å^3)	147.02	119.53	107.28	99.21
	Energy, E_{FM} (eV)	−4570.77	−4570.05	−4568.85	−4567.53
	Energy, E_{AFM} (eV)	−4570.75	−4570.02	−4568.80	−4567.45
	Energy, E_{NM} (eV)	−4568.31	−4567.76	−4566.72	−4565.47
	Normalized lattice constants a/a_0	1	0.93	0.89	0.87
	Normalized volume V/V_0	1	0.80	0.71	0.66
$FrCrBr_3$	Lattice constant a (Å)	5.43	5.05	4.86	4.73
	Non-spin polarized $a/b/c$ (Å)	5.32	4.96	4.78	4.66
	Cell volume, V_0 (FM) (Å^3)	160.53	128.43	114.52	105.68
	Cell volume, V_0 (NM) (Å^3)	150.54	121.99	109.40	101.08
	Energy, E_{FM} (eV)	−4990.58	−4989.86	−4988.62	−4987.27
	Energy, E_{AFM} (eV)	−4990.55	−4989.82	−4988.58	−4987.21
	Energy, E_{NM} (eV)	−4988.09	−4987.52	−4986.46	−4985.19
	Normalized lattice constants a/a_0	1	0.93	0.90	0.87
	Normalized volume V/V_0	1	0.80	0.71	0.66

Table 2 Formation and cohesive energies calculated at applied pressures of 0, 10, 20, and 30 GPa for $ACrBr_3$ (A = K, Rb, Cs, Fr) compounds

		Pressure			
Energy, (eV)	Compounds	0 GPa	10 GPa	20 GPa	30 GPa
$E_{Formation}$	$KCrBr_3$	−2.75, −2.65[29]	−3.39	−2.42	−2.44
	$RbCrBr_3$	−2.77, −2.21[30]	−3.46	−2.49	−2.48
	$CsCrBr_3$	−2.80	−3.52	−2.45	−2.34
	$FrCrBr_3$	−2.76	−3.47	−2.47	−2.36
$E_{Cohesive}$	$KCrBr_3$	12.96	10.53	11.96	12.02
	$RbCrBr_3$	12.64	11.62	12.02	12.52
	$CsCrBr_3$	12.78	11.5	11.79	11.76
	$FrCrBr_3$	12.84	11.14	11.79	11.82

in a cubic lattice can be written using the following expression, as it has only distinct elastic constants (C_{11}, C_{12} and C_{44}):[40]

$$U_{elastic} = \frac{1}{2}V_0\left[(C_{11}-C_{12})\left(e_1^2+e_2^2+e_3^2\right)+C_{12}(e_1+e_2+e_3)^2 + C_{44}\left(e_4^2+e_5^2+e_6^2\right)\right]+O\left(e^3\right). \quad (6)$$

Here V_0 is the unstrained volume and $O(e^3)$ is the strain order e^3 or higher. Only when this energy becomes positive, the crystal structure has dynamical stability. For this reason, Born stability requirements, which are $(C_{11}-C_{12})>0$; $C_{11}+2C_{12}>0$; $C_{44}>0$; $C_{11}>0$, must be followed for a cubic crystal structure to become a mechanically stable structure.[41] All our studied compounds are mechanically stable, as shown in Table 4. We also analyzed these constants across various pressures, with the goal of better understanding the impact of pressure on various mechanical properties, to know the dynamical stability of our compounds, which are shown in Table 4. The pressure-induced stability condition is:[42] $C_{11}-C_{12}-2P>0$; $C_{12}+2C_{12}>0$; $C_{44}-P>0$. The pressure-induced stability criteria are not satisfied for $KCrBr_3$ at 30 GPa. However, the other compounds within the applied pressure range maintain dynamical stability.

Table 4 and Fig. 5 show that all three elastic constants for our studied materials increase with increasing pressure. For technological and industrial purposes, Young's modulus is an essential factor when studying the rigidity of any material.[43]

$$Y=\frac{9BG}{3B+G} \quad (7)$$

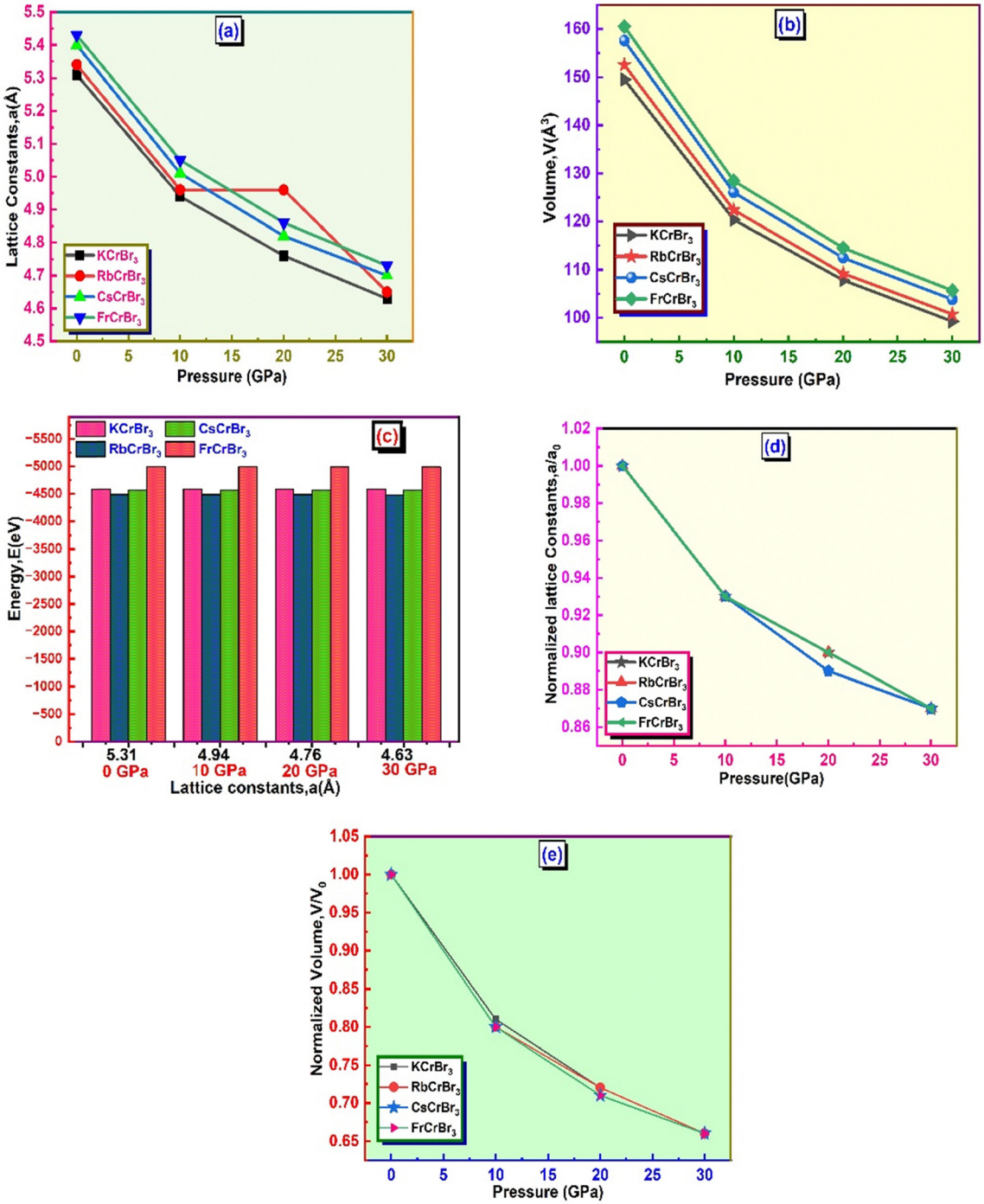

Fig. 2 Pressure-dependent variation of (a) lattice constants a (Å), (b) volume V_0 (Å^3), (c) total energies (eV), (d) normalized lattice constants, and (e) normalized volume for $ACrBr_3$ (A = K, Rb, Cs, Fr) calculated using the GGA-PBE functional at pressures of 0, 10, 20, and 30 GPa.

From Table 5 and Fig. 6, it is observed that as pressure increases, the value Y also rises for all materials, meaning our materials become stiffer with the applied pressure. Among the materials we examined, Fr-based perovskites exhibit the highest stiffness as well as structural integrity in the pressure range of 0–30 GPa and can better resist the applied deformation.

From our calculated values of B (30.75–32.74 GPa) without applied pressure, it is found that our materials may be used in a thin film solar cell because of their flexibility and softness.[44] The following equations can be utilized to describe G_V and G_R from the Voigt and Reuss assumptions using the elastic constants.

$$B = \frac{1}{3}(C_{11} + 2C_{12}) \quad (8)$$

$$G_V = \frac{C_{11} - C_{12} + 3C_{44}}{5} \quad (9)$$

Table 3 Tolerance factor (t), octahedral factor (μ), bond lengths (Å), bond populations and Mulliken charges (electrons) of $ACrBr_3$ (A = K, Rb, Cs, Fr) from the GGA-PBE functional at 0 GPa

Compounds	Tolerance factor (t)	Octahedral factor (μ)	Bond	Population	Bond lengths (Å)	Species	s	p	d	Total	Charge (electrons)
$KCrBr_3$	0.99	0.52	Cr–Br	−0.43	2.65	K	2.29	6.66	0	8.94	0.06
						Cr	2.65	6.91	4.71	14.27	−0.27
						Br	1.53	5.40	0	6.93	0.07
$RbCrBr_3$	1.01	0.52	Cr–Br	−0.47	2.67	Rb	2.28	6.61	0	8.89	0.11
						Cr	2.61	6.91	4.70	14.22	−0.22
						Br	1.56	5.41	0	6.96	0.04
$CsCrBr_3$	1.05	0.52	Cr–Br	−0.26	2.70	Cs	2.28	6.49	0	8.77	0.23
						Cr	2.57	6.88	4.68	14.14	−0.14
						Br	1.61	5.42	0	7.03	−0.03
$FrCrBr_3$	1.07	0.52	Cr–Br	−0.21	2.72	Fr	2.26	6.43	0	8.69	0.31
						Cr	2.56	6.87	4.67	14.10	−0.10
						Br	1.65	5.42	0	7.07	−0.07

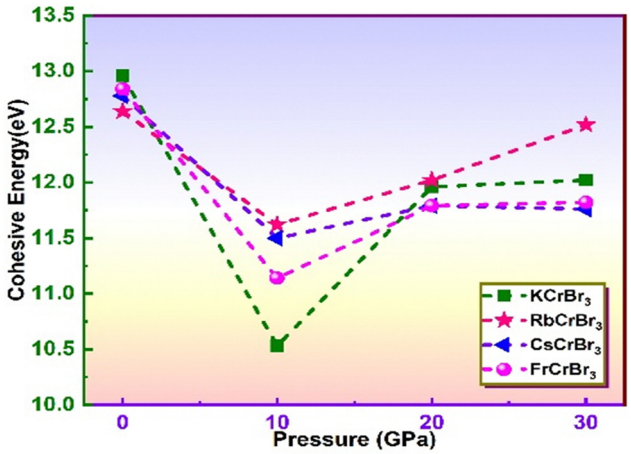

Fig. 3 Variation of cohesive energy for $ACrBr_3$ (A = K, Rb, Cs, Fr) compounds under applied pressures of 0, 10, 20, and 30 GPa.

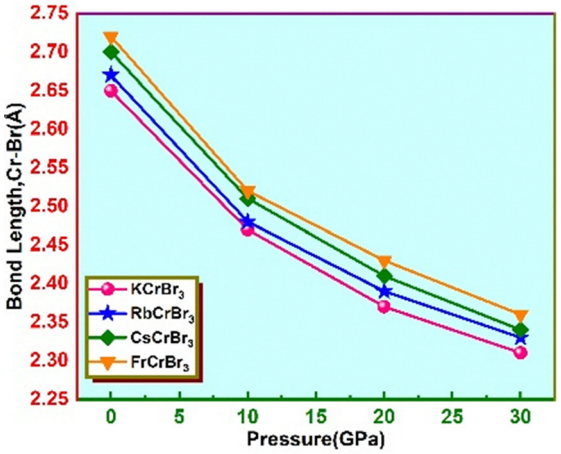

Fig. 4 Pressure-dependent variation of bond length (Å) for $ACrBr_3$ (A = K, Rb, Cs, Fr) perovskites calculated using the GGA-PBE functional.

$$G_R = \frac{5(C_{11} - C_{12})C_{44}}{4C_{44} + 3(C_{11} - C_{12})} \quad (10)$$

From the Hill[45] concept, we can determine the shear modulus G of a crystal lattice from G_V and G_R as:

$$G = \frac{G_R + G_V}{2} \quad (11)$$

The ability of a material to resist shear deformation is known as the shear modulus. $FrCrBr_3$ shows the highest shear modulus among our other investigated compounds with and without applied pressure, as seen from Table 5 and Fig. 6. Without applied pressure, our materials may be used in flexible electronics. The elastic constants show that, without applied pressure and under most pressures, $Y > B > G$ except for $KCrBr_3$ and $CsCrBr_3$ above 10 GPa pressure. So our materials show a greater tendency of linear deformation over volumetric contraction. Due to the increase of Y, B, and G with pressure, our materials become harder with pressure. Using ν, we can assess the bonding nature of the compound. If ν = 0.25, then it means that there exists an ionic bond, if $\nu > 0.25$, then the bond is metallic, and if $\nu < 0.25$, then a covalent bond is anticipated.[43] K- and Rb-based materials show metallic bonds under all our investigated pressures, whereas Cs- and Fr-based materials show ionic bonds at 0 GPa pressure, which turn into metallic bonds under pressure.

$$\nu = \frac{3B - 2G}{2(3B + G)} \quad (12)$$

Ductile materials have potential applications in flexible electronics as well as photovoltaic cells, as the ability to sustain mechanical deformation without fracturing is needed.[46] Also, ductility and brittleness can be identified by this parameter. If $\nu > 0.26$ then the material is ductile. The pressure effect on this value can be visualized from Table 5 and Fig. 6, which shows that pressure can enhance the ductility of our studied compounds. The value of Pugh's ratio (B/G) tells us whether our studied compounds are ductile or brittle. If this value remains less than 1.75, then the

Table 4 Elastic stiffness constants C_{ij} (GPa), Born stability, and dynamical stability criteria of $ACrBr_3$ (A = K, Rb, Cs, Fr) compounds using the GGA-PBEsol functional at applied pressures of 0, 10, 20, and 30 GPa

		Elastic stiffness constants			Born stability				Dynamical stability		
Compounds	Pressure, P	C_{11}	C_{12}	C_{44}	$C_{11} - C_{12} > 0$	$C_{11} + 2C_{12} > 0$	$C_{11} > 0$	$C_{44} > 0$	$C_{11} - C_{12} - 2P > 0$	$C_{11} + 2C_{12} > 0$	$C_{44} - P > 0$
$KCrBr_3$	0	61.98, 64.21[29]	18.12, 42.30[29]	14.20, 3.98[29]	43.86	98.22	61.98	14.20	43.86	98.22	14.2
	10	145.91	38.17	19.65	107.74	222.25	145.91	19.65	87.74	222.25	9.65
	20	217.82	59.62	24.5	158.2	337.06	217.82	24.5	118.2	337.06	4.5
	30	279.96	77.64	27.16	202.32	435.24	279.96	27.16	142.32	435.24	−2.84
$RbCrBr_3$	0	59.79	16.23	13.91	43.56	92.25	59.79	13.91	43.56	92.25	13.91
	10	148.84	40.14	22.49	108.7	229.12	148.84	22.49	88.7	229.12	12.49
	20	220.26	61.85	30.77	158.41	343.96	220.26	30.77	118.41	343.96	10.77
	30	287.59	80.29	35.63	207.3	448.17	287.59	35.63	147.3	448.17	5.63
$CsCrBr_3$	0	60.04	17.96	17.51	42.08	95.96	60.04	17.51	42.08	95.96	17.51
	10	145.06	41.85	28.16	103.21	228.76	145.06	28.16	83.21	228.76	18.16
	20	219.61	63.33	38.79	156.28	346.27	219.61	38.79	116.28	346.27	18.79
	30	287.59	84.17	47.36	203.42	455.93	287.59	47.36	143.42	455.93	17.36
$FrCrBr_3$	0	58.65	19.13	18.5	39.52	96.91	58.65	18.5	39.52	96.91	18.5
	10	140.76	44.24	31.56	96.52	229.24	140.76	31.56	76.52	229.24	21.56
	20	215.11	66.48	42.31	148.63	348.07	215.11	42.31	108.63	348.07	22.31
	30	281.77	86.71	52.38	195.06	455.19	281.77	52.38	135.06	455.19	22.38

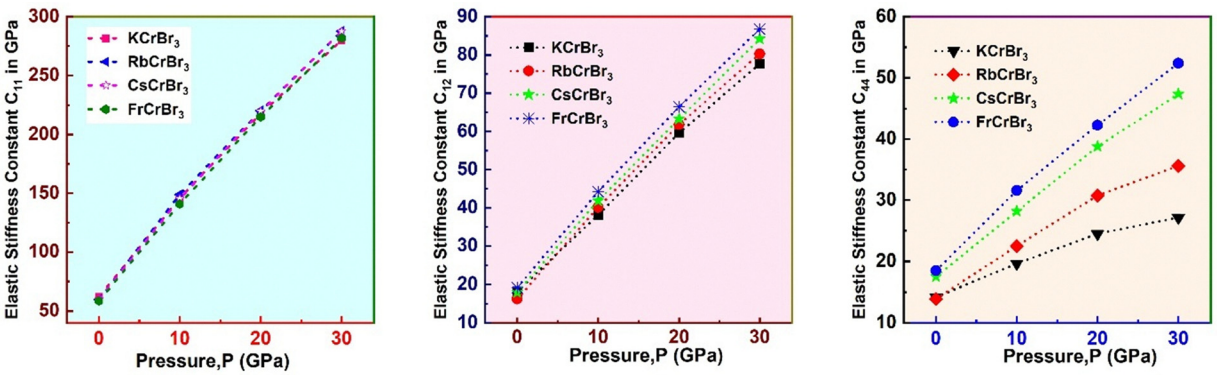

Fig. 5 Variation of elastic stiffness constants C_{11}, C_{12}, and C_{44} (GPa) with pressure using the GGA-PBEsol functional for $ACrBr_3$ (A = K, Rb, Cs, Fr) compounds.

materials are brittle; otherwise, they show a ductile nature. $CsCrBr_3$ and $FrCrBr_3$ at 0 GPa pressure show a value less than this value, meaning they are brittle under ambient conditions. With the application of external pressure, they start to show ductility, meaning that pressure increases this ratio significantly.

$$C_p = C_{12} - C_{44} \quad (13)$$

The Cauchy pressure, C_p in eqn (13), is another factor which is also used to differentiate between ductile and brittle materials. From Table 5, it is found that pressure increases the ductility of our studied materials. All three parameters ν, B/G, and C_p show a similar ductile or brittle nature. The Zener anisotropy[47] index A can be used for determining the anisotropy of cubic crystals, that is:

$$A = \frac{2C_{44}}{C_{11} - C_{12}} \quad (14)$$

If $A = 1$, then the structure is isotropic, meaning the material is the same in all directions, and having any value other than 1 means the material is anisotropic.[48] The value of this parameter gradually drops from unity under applied pressure, which suggests that all of our materials turn more anisotropic. Vickers hardness H_V is calculated using the following formula:[49]

$$H_V = \frac{[(1-2\nu)E]}{6(1+\nu)} \quad (15)$$

H_V has an important role in making cutting instruments, coatings, building materials, and wear-resistant parts and in other industries. A high value of H_V means the material can withstand plastic deformation, and this parameter is increased with the applied pressure for all our investigated materials, as seen from Fig. 6 and Table 5. The Kleinman parameter ζ has the following expression:

$$\zeta = \frac{C_{11} + 8C_{12}}{7C_{11} + 2C_{12}} \quad (16)$$

It falls between 0 and 1. If $\zeta = 0$, the bond is stretching and $\zeta = 1$ denotes the bending bond. The calculated values of ζ with changes in pressure are shown in Table 5. It has a vital role in designing semiconductors with certain optical and electrical characteristics

Table 5 Various elastic constants calculated using the GGA-PBEsol functional for $ACrBr_3$ (A = K, Rb, Cs, Fr) compounds under applied pressures of 0, 10, 20, and 30 GPa

Compounds	Pressure, P	Young's modulus (Hill) Y	Bulk modulus (B)	Shear modulus (Voigt) G_V	Shear modulus (Reuss) G_R	Shear modulus (Hill) (G)	Cauchy pressure (C_p)	Kleinman parameter (ξ)	Anisotropy factor (A)	Poisson ratio (ν)	Pugh's ratio (B/G)	Vickers hardness, H_V	Machinability index, μ_m
$KCrBr_3$	0	43.28	32.74	17.29	16.53	16.91	3.92	0.44, 0.75[29]	0.65, 0.36[29]	0.28, 0.44[29]	1.94, 8.19[29]	2.48	2.31
	10	78.93	74.08	33.34	26.34	29.84	18.52	0.411	0.36	0.32	2.48	3.53	3.77
	20	107.49	112.35	46.34	33.84	40.09	35.12	0.42	0.31	0.34	2.8	4.26	4.59
	30	128.67	145.08	56.76	38.39	47.58	50.48	0.43	0.27	0.35	3.05	4.69	5.34
$RbCrBr_3$	0	42.33	30.75	17.06	16.26	16.66	2.32	0.42	0.64	0.27	1.85	2.55	2.21
	10	84.94	76.37	35.23	29.38	32.31	17.65	0.42	0.41	0.31	2.36	3.99	3.40
	20	120.41	114.65	50.14	40.73	45.44	31.08	0.43	0.39	0.32	2.52	5.30	3.73
	30	148.33	149.39	62.83	48.31	55.57	44.66	0.43	0.34	0.33	2.69	6.13	4.19
$CsCrBr_3$	0	47.26	31.99	18.92	18.77	18.85	0.45	0.45	0.83	0.25	1.70	3.09	1.83
	10	93.26	76.25	37.54	34.41	35.98	13.69	0.44	0.54	0.30	2.12	4.89	2.71
	20	134.62	115.42	54.53	48.57	51.55	24.54	0.44	0.50	0.31	2.24	6.68	2.98
	30	169.90	151.98	69.1	60.23	64.67	36.81	0.44	0.47	0.31	2.35	8.03	3.21
$FrCrBr_3$	0	47.64	32.30	19.00	18.98	18.99	0.63	0.47	0.94	0.25	1.70	3.11	1.75
	10	96.54	76.41	38.24	36.63	37.44	12.68	0.46	0.65	0.29	2.04	5.26	2.42
	20	138.25	116.02	55.11	51.11	53.11	24.17	0.46	0.57	0.30	2.18	7.03	2.74
	30	176.03	151.73	70.44	64.28	67.36	34.33	0.45	0.54	0.31	2.25	8.68	2.90

that can be used in LEDs or photonic devices.[50] The machinability index can be calculated from the following relation:[51]

$$\mu_m = \frac{B}{C_{44}} \quad (17)$$

The value of μ_m is greater than 2 except for the Cs and Fr based compounds, which remain below 2 at 0 GPa. When the pressure is applied, this value is also enhanced. Exceeding a machinability index of 2 demonstrates outstanding lubrication property and smaller friction and is suitable for industrial uses.

3.3 Electronic characteristics

Electronic property analysis plays an important role in determining the applicability of the halide perovskites in various fields. Spin-polarized band structures, density of states (DOS), and partial density of states (PDOS) have been investigated for all of our materials over a pressure range of 0 to 30 eV. Fig. 7 presents our examined band structures in both spin-up and spin-down states along the high symmetry points G–F–Q–Z–G in the Brillouin zone using both GGA and GGA+U functionals. The band gap values of d/f electron-based systems are underestimated by GGA. We have used GGA+U, where the Hubbard potential is 2.50 eV for the Cr atom.[52] The band gap value is enhanced by including the U parameter, which takes it significantly closer to the experimental values.[53] The Fermi level E_F is set at 0 eV in the horizontal line. The conduction band is situated above this line, whereas the valence band is situated below. In spin-up states (↑), all of our studied materials show metallic nature, as there exist some bands in the Fermi level in both the GGA and GGA+U functionals. In the spin down state (↓), there exists a band gap E_g between the valence and conduction bands, and the band gap values are shown in Table 6 and Fig. 7. Our studied materials over the pressure range can be classified as half metals because of their two different nature in spin up and down states. In the spin down state, the valence band maximum (VBM) and conduction band minimum (CBM) lie at points Q and G, respectively, so our studied compounds possess an indirect band gap for all investigated pressure ranges. Pressure has a vital effect on the band structure. From Fig. 8, with the applied pressure, all of our materials show a decrease in band gap with the applied pressure. At 30 GPa, all of our materials exhibit metallic behavior in the spin-up channel and a wide-band-gap semiconducting nature in the spin-down channel, thereby maintaining half-metallicity, which is useful in electronic and optoelectronic applications for their high optical phonon energies. The half-metallic gap is defined as the minimum energy difference between the Fermi level and the nearest band edge, either the valence band maximum or the conduction band minimum.[54] Mathematically, $E_{HM} = \min[(E_F - E_{VBM}), (E_{CBM} - E_F)]$, where E_F is the Fermi level, E_{VBM} is the valence band maximum, E_{CBM} is the conduction band minimum and E_{HM} is the lowest quantity of energy needed to create holes in the minority spin channel and create spin excitation.[15] According to Table 6 our calculated half-metallic gap is large enough for spintronic applications[55] like spin field-effect transistors, magnetoresistive-based devices, and racetrack memory.[56]

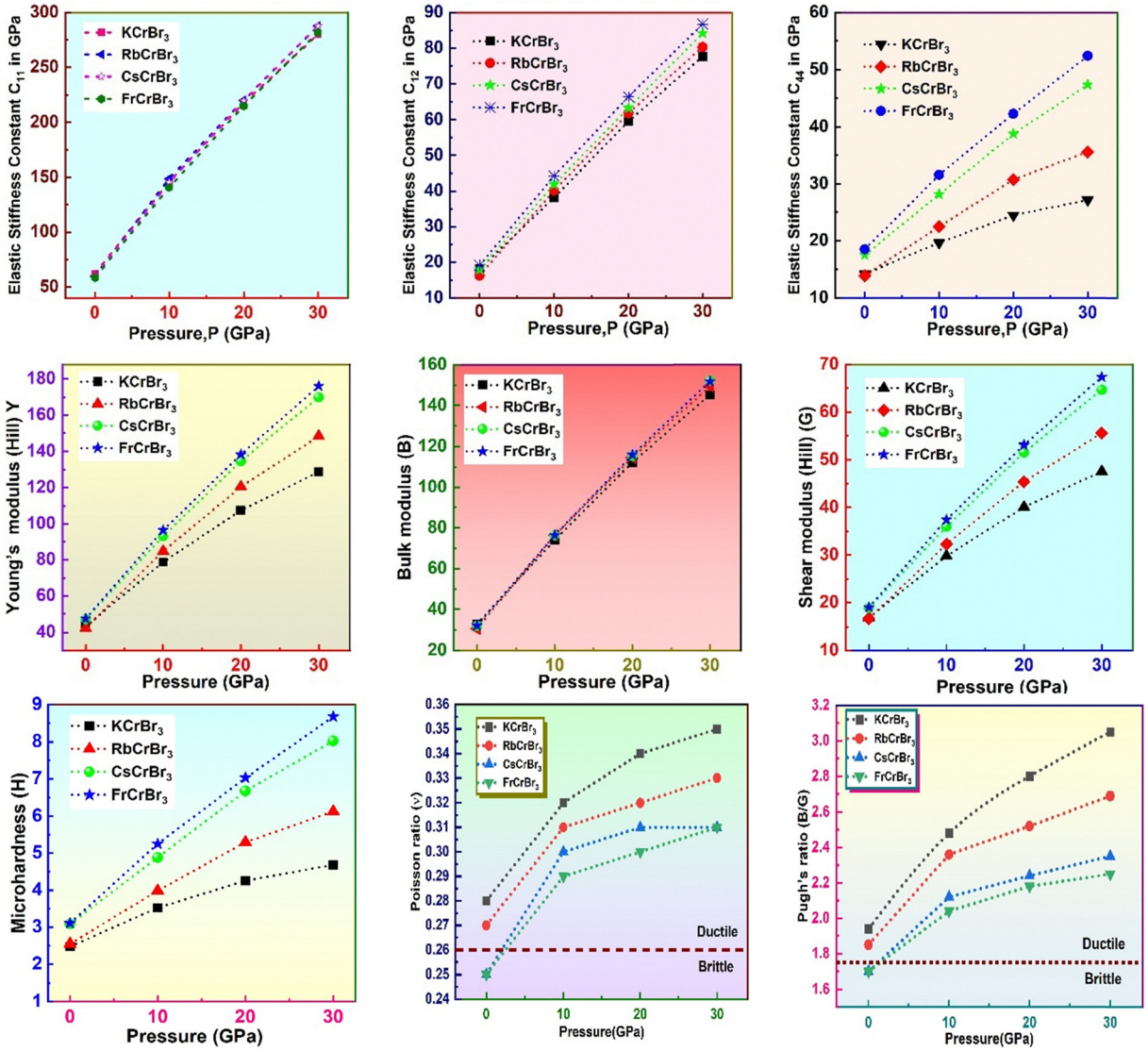

Fig. 6 Calculated various elastic moduli and their variation with pressure (GPa) using the GGA-PBEsol functional for $ACrBr_3$ (A = K, Rb, Cs, Fr).

Density of states (DOS) and partial density of states (PDOS) are also investigated to further evaluate the half-metallicity. $ACrBr_3$ (A = K, Rb, Cs, Fr) exhibit half-metallic behavior, determined using both GGA and GGA+*U*, as the spin-up channel shows metallic states at the Fermi level while the spin-down channel shows a gap as depicted by the DOS structure over 0–30 GPa in Fig. 9 using GGA and GGA+*U*. From PDOS using the GGA+*U* functional at 0 GPa, the states around E_F mainly arise from Cr-3d and Br-4p hybridization, as illustrated in Fig. 10, and this hybridization makes our studied materials a half metal. At elevated pressure, the minority-spin gap narrows as hybridization becomes stronger.

3.4 Spin polarization

The spin polarization is related to the spin-polarized DOS by the following formula:[11]

$$\text{Spin-polarization, SP}\ (\%) = \frac{\rho\uparrow(E_F) - \rho\downarrow(E_F)}{\rho\uparrow(E_F) + \rho\downarrow(E_F)} \times 100 \quad (18)$$

Here $\rho\uparrow(E_F)$ and $\rho\downarrow(E_F)$ denote the majority and minority spin density at the Fermi level. If $\rho\uparrow(E_F) = 0$ or $\rho\downarrow(E_F) = 0$, it means any one of the spin states is responsible for electron movement and maximum SP occurs. All of our materials have 100% SP at the Fermi level, which further illustrates the half-metallic characteristics.

3.5 Magnetic properties and Curie temperature

Magnetic properties of our compounds are investigated using GGA and GGA+*U* functionals. Table 7 and Fig. 11 illustrate the total and atomic magnetic moments in Bohr magnetons (μ_B). The total magnetic moment is calculated by using the following formula:

$$\mu_T = \text{A (A = K, Rb, Cs, Fr)} + \text{Cr} + 3\text{Br} \quad (19)$$

The calculated total magnetic moments range from 3.98 to 4.02 and −3.99, which are either integer or nearly integer values. Such values verify that all our investigated materials are ferromagnetic.[57] Only the Cr atom significantly contributes to

the magnetic moment, whereas other atoms make a negligible contribution. From the Slater–Pauling (SP) rule, the total magnetic moment (μ_T) per unit cell for transition-metal-based half-metallic materials is,

$$\mu_T = Z_T - 24 \quad (20)$$

where Z_T denotes the total number of valence electrons in our material. In our compounds $ACrBr_3$ (A = K, Rb, Cs, Fr), A-site materials (K, Rb, Cs, and Fr) have 1 valence electron, chromium has 6 valence electrons ($3d^5\ 4s^1$), and the bromine ([Ar] $4s^2\ 3d^{10}\ 4p^5$) atom has 7 valence electrons. So, $Z_T = 1(A) + 6(Cr) + 3 \times 7(Br) = 28$ electrons and $\mu_T = (28 - 24) = 4\mu_B$, consistent with our results derived from individual atomic contributions.

The temperature above which spontaneous magnetization of a material is lost is known as the Curie temperature. We can evaluate the Curie temperature by using the following formula,[58]

$$T_C = \frac{2}{3k_B}(E_{AFM} - E_{FM}) \quad (21)$$

Here, k_B denotes the Boltzmann constant and E_{FM} and E_{AFM} represent the total energies of the ferromagnetic and antiferromagnetic states, respectively. The calculated Curie temperature and pressure effect are shown in Table 8 and Fig. 12. Applied pressure leads to an increase in the estimated Curie temperature for all compounds at all pressures, except for the $KCrBr_3$ compound at 10 GPa, where the T_C value shows a decrease.

3.6 Thermal properties

The investigation of thermal properties is essential to understand how energy and heat behave, interact, and transform within solid materials. By employing the calculated elastic constants, the Debye temperature, θ_D, can be determined by the following expressions:

$$\theta_D = \frac{h}{k_B}\left[\frac{3n}{4\pi}\left(\frac{N_A\rho}{M}\right)\right]^{1/3} v_m \quad (22)$$

$$v_m = \left[\frac{1}{3}\left(\frac{2}{v_t^3} + \frac{1}{v_l^3}\right)\right]^{-\frac{1}{3}} \quad (23)$$

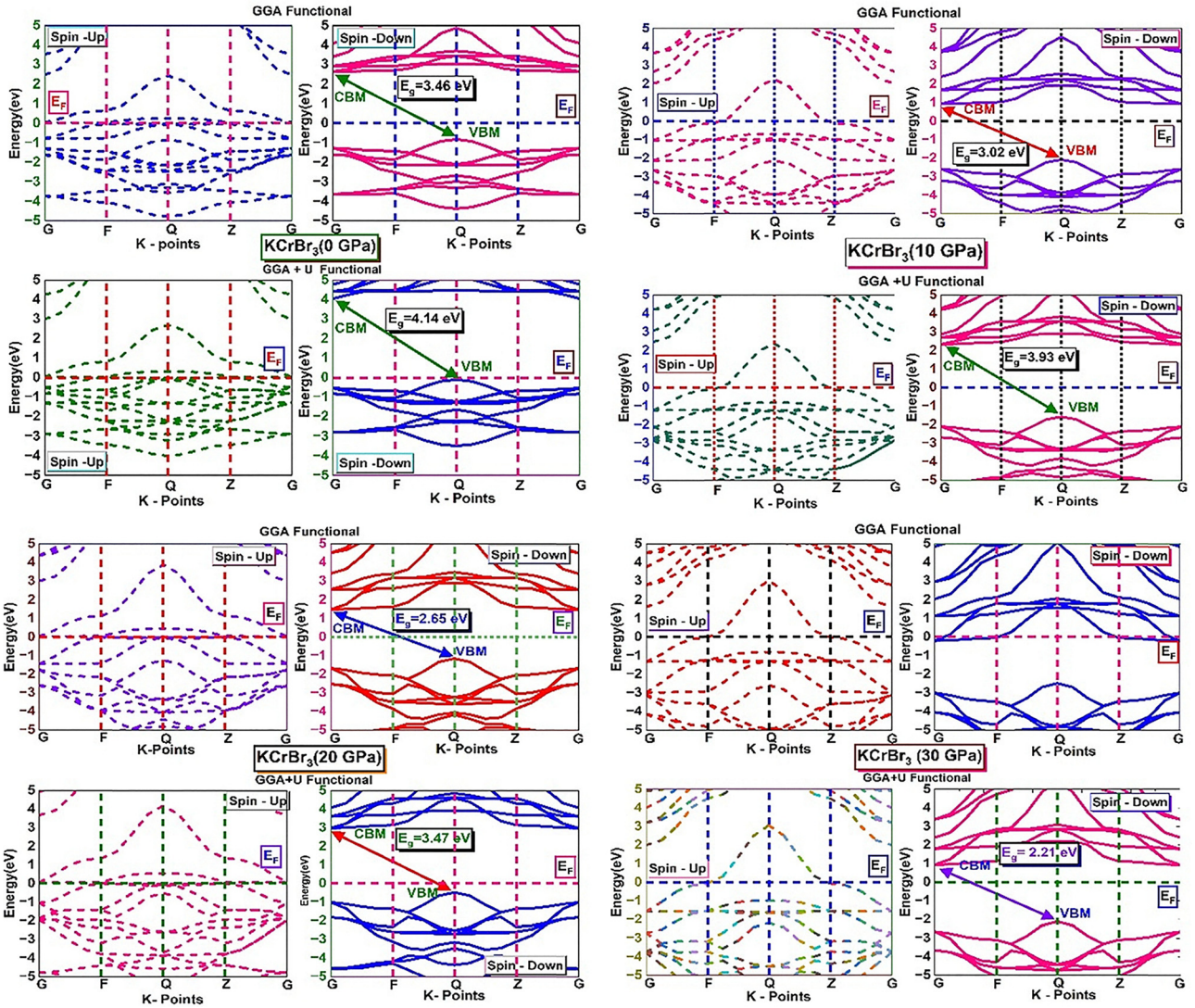

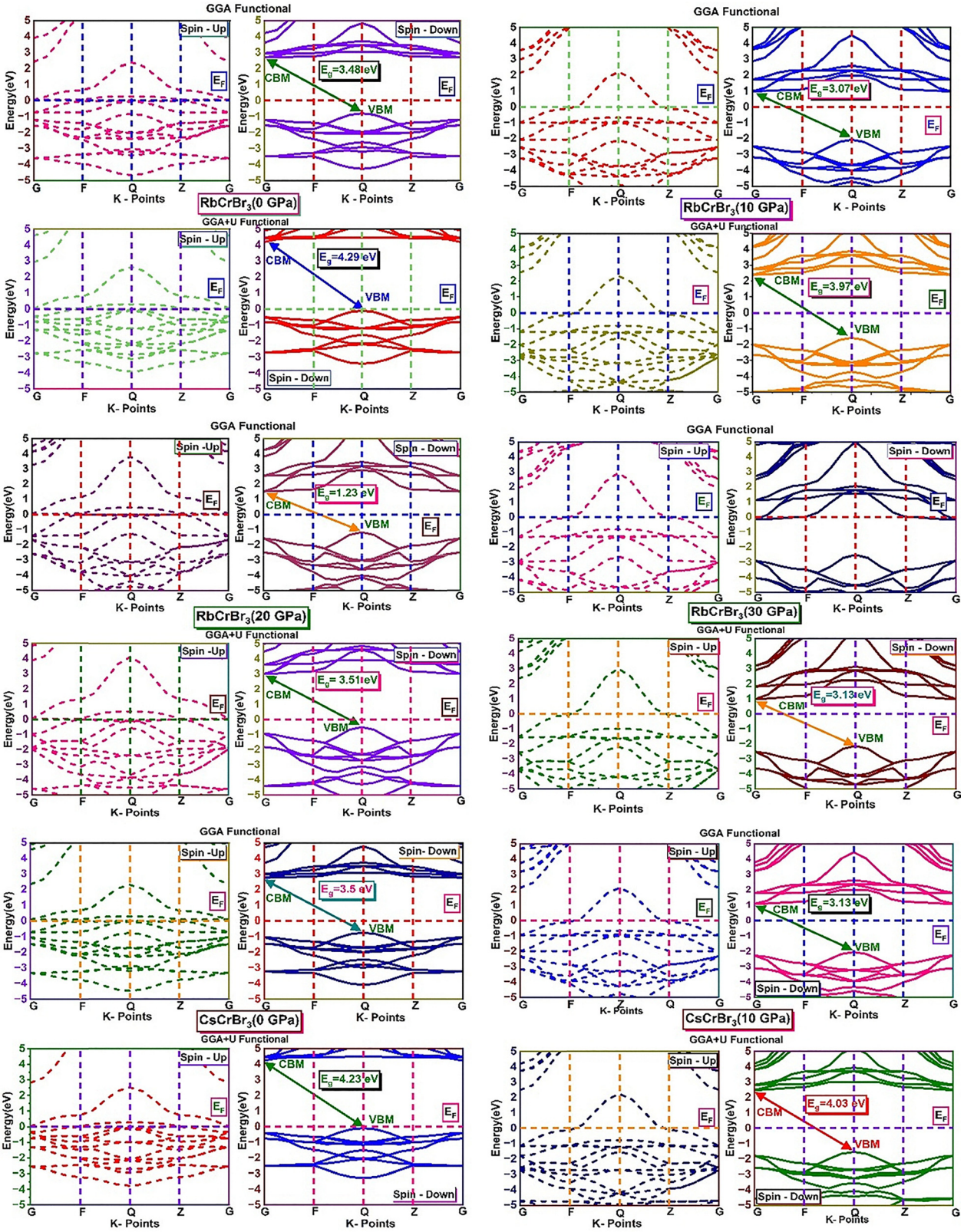

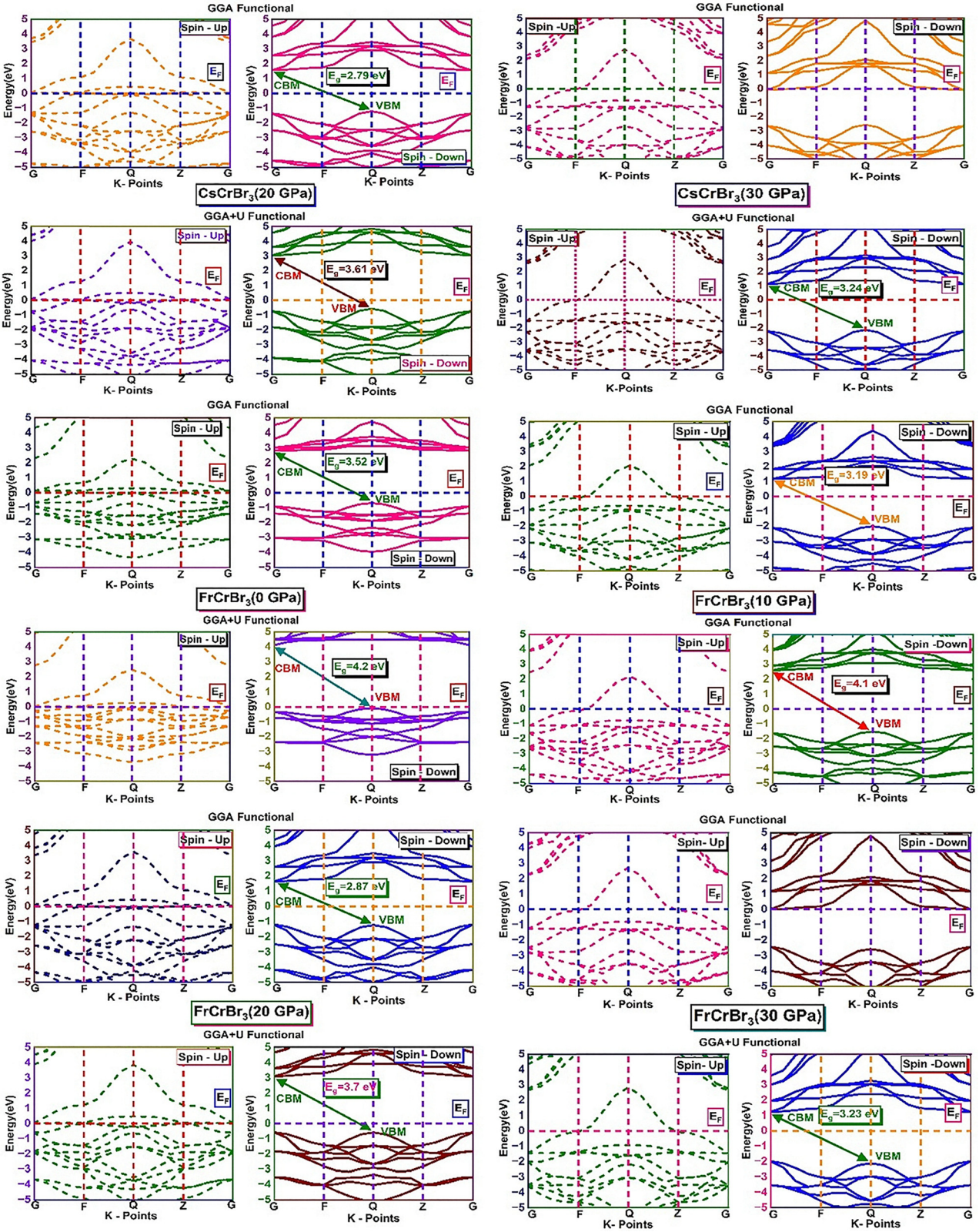

Fig. 7 Spin-polarized band structures of $ACrBr_3$ (A = K, Rb, Cs, Fr) obtained from GGA-PBE and GGA+*U* functionals at applied pressures of 0, 10, 20, and 30 GPa.

Table 6 Calculated minority-spin band gaps (eV) and half-metallic gaps (eV) using GGA and GGA+U functionals at applied pressures of $ACrBr_3$ (A = K, Rb, Cs, Fr) compounds

		Band gap, E_g (eV)			
		GGA		GGA+U	
Halide perovskites	Pressure (GPa)	Spin-down band gap	Half-metallic gap	Spin-down band gap	Half-metallic gap
$KCrBr_3$	0	3.46, 3.4[29]	0.82, 0.3[29]	4.14	0.103
	10	3.02	0.94	3.93	1.59
	20	2.65	1.16	3.47	0.48
	30	—	—	2.21	0.09
$RbCrBr_3$	0	3.48	0.79	4.29	0.1
	10	3.07	1	3.97	1.57
	20	1.231	0.05	3.51	0.51
	30	—	—	3.13	1
$CsCrBr_3$	0	3.5	0.74	5.14	0.91
	10	3.13	1.09	4.03	1.54
	20	2.79	1.22	3.61	0.56
	30	—	—	3.24	1.11
$FrCrBr_3$	0	3.52	0.7	4.2	0.09
	10	3.19	1.17	4.1	1.51
	20	2.87	1.23	3.7	0.59
	30	—	—	3.23	1.23

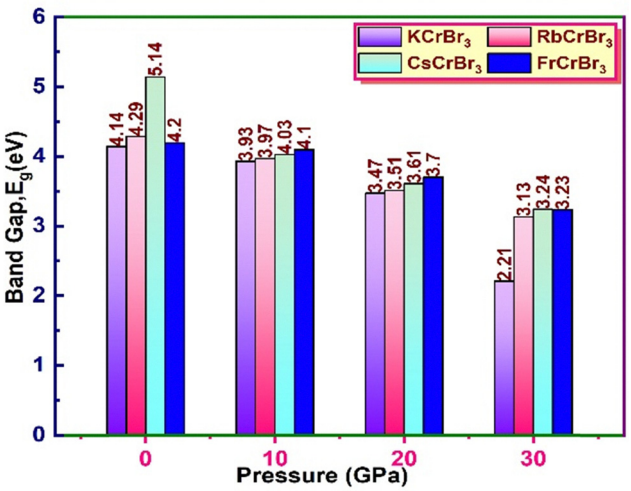

Fig. 8 Variation of band gap (eV) with applied pressures of 0, 10, 20, and 30 GPa for $ACrBr_3$ (A = K, Rb, Cs, Fr) compounds using the GGA+U functional.

From Navier's equation,[59]

$$v_t = \sqrt{\frac{G}{\rho}} \tag{24}$$

$$v_l = \sqrt{\frac{B + \frac{4G}{3}}{\rho}} \tag{25}$$

Here, θ_D denotes the Debye temperature, h stands for Planck's constant, k_B is Boltzmann's constant, n is the number of atoms in the molecule, N_A is Avogadro's number, M is the molecular weight, ρ is the density, and v_m is the average sound velocity. With the application of pressure, the value of B and G increases, which results in an increase in average sound velocity as seen from Table 9. As a result, Debye temperature also increases with the increase of applied pressure. This high value of Debye temperature suggests that our materials are expected to have high melting points, high hardness, and large thermal expansion coefficients and might be applied to thermal resistance materials. The temperature at which a solid melt into a liquid under normal atmospheric pressure is known as the melting temperature and has the following expression:

$$T_{melting} = 553 + \left(\frac{5.91\ \text{K}}{\text{GPa}}\right) C_{11} \tag{26}$$

Applying pressure results in an increase in the melting temperature of all our investigated materials as seen from Fig. 13. The Debye frequency represented by ω_D, gives information on the transmission of heat at the atomic scale and can be calculated using the following expression:[60]

$$\omega_D = \frac{k_B \times \theta_D}{h} \tag{27}$$

With the increase in pressure, the value of ω_D also increases, resulting in greater heat capacity as well as thermal conductivity. The highest value is shown for Cs based compounds, illustrated in Table 9. The minimum thermal conductivity (K_{min}) can be computed from the Clarke formula, which is:[61]

$$K_{min} = k_B v_m \left(\frac{M}{nN_A\rho}\right)^{-2/3} \tag{28}$$

The application of pressure enhances K_{min}, hence Rb and Cs based materials exhibit the highest values at 30 GPa pressure, as shown in Table 9.

3.7 Optical properties

Investigating the optical properties of materials is essential, as it lets us know how they react to incident electromagnetic radiation. This understanding is critical for the design and selection of materials used in optoelectronic device applications. Fig. 14 shows the optical properties, absorption, energy loss, real and imaginary dielectric constants, refractive index, real optical conductivity, and optical reflectivity of our compounds $ACrBr_3$ (A = K, Rb, Cs, Fr) in the 0–30 eV photon energy range under applied pressures of 0, 10, 20, and 30 GPa. Primarily, we can describe a material's response to electromagnetic radiation as its dielectric function. The complex dielectric function, $\varepsilon(\omega)$, can be found by the following equation:

$$\varepsilon(\omega) = \varepsilon_1(\omega) + i\varepsilon_2(\omega) \tag{29}$$

Here, $\varepsilon_1(\omega)$ is the real part and $\varepsilon_2(\omega)$ is the imaginary part of the complex dielectric function. The degree of charge recombination is demonstrated by the dielectric function's static value $\varepsilon_1(0)$, which is related to the manner in which optoelectronic devices perform. The real static dielectric constant $\varepsilon_1(0)$ is highest when the photon energy is 0 eV, and its value is

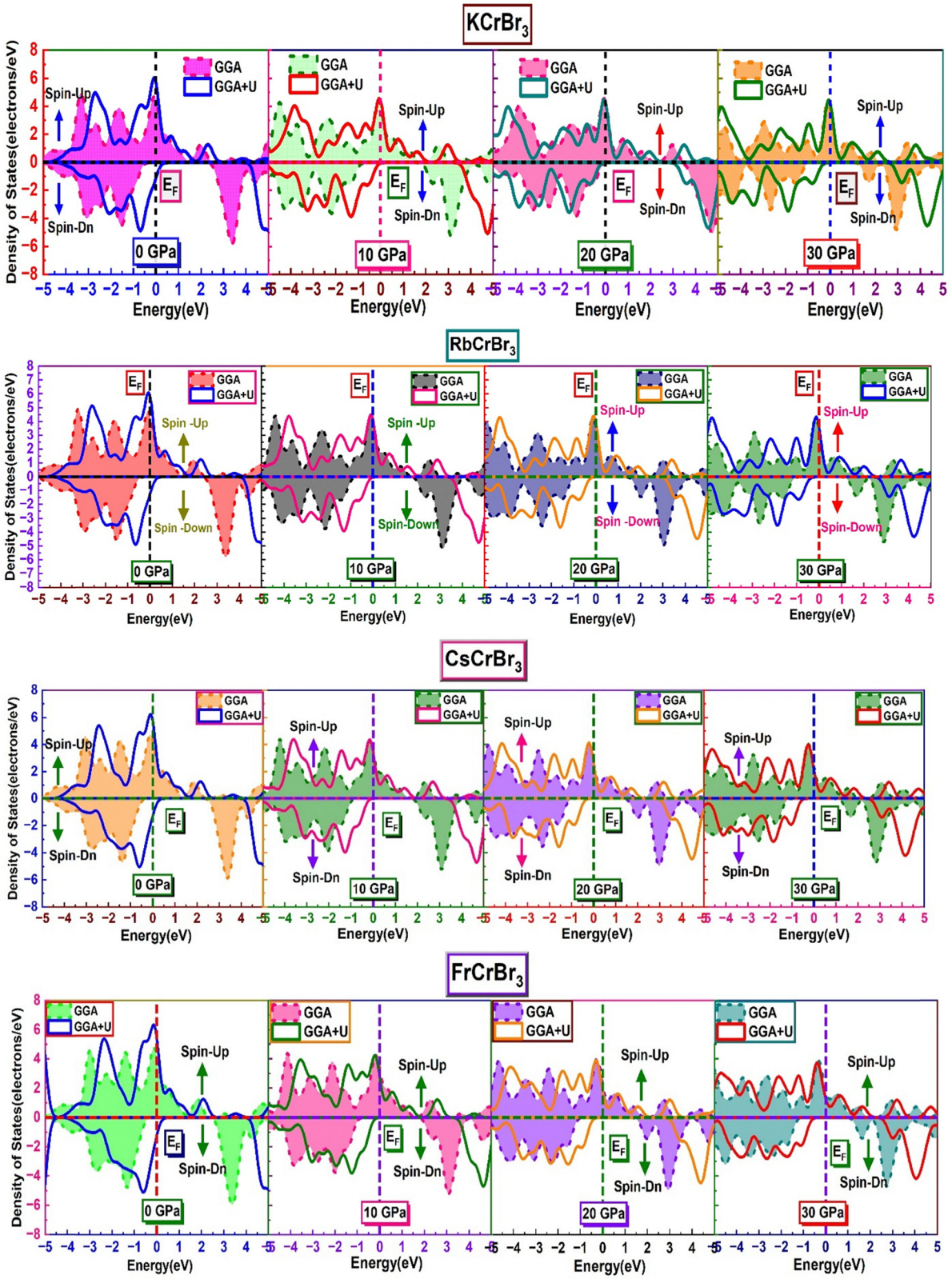

Fig. 9 Spin-polarized density of states (DOS) (electrons per eV) of $ACrBr_3$ (A = K, Rb, Cs, Fr) perovskites using the GGA and GGA+*U* functionals under applied pressures of 0, 10, 20, and 30 GPa.

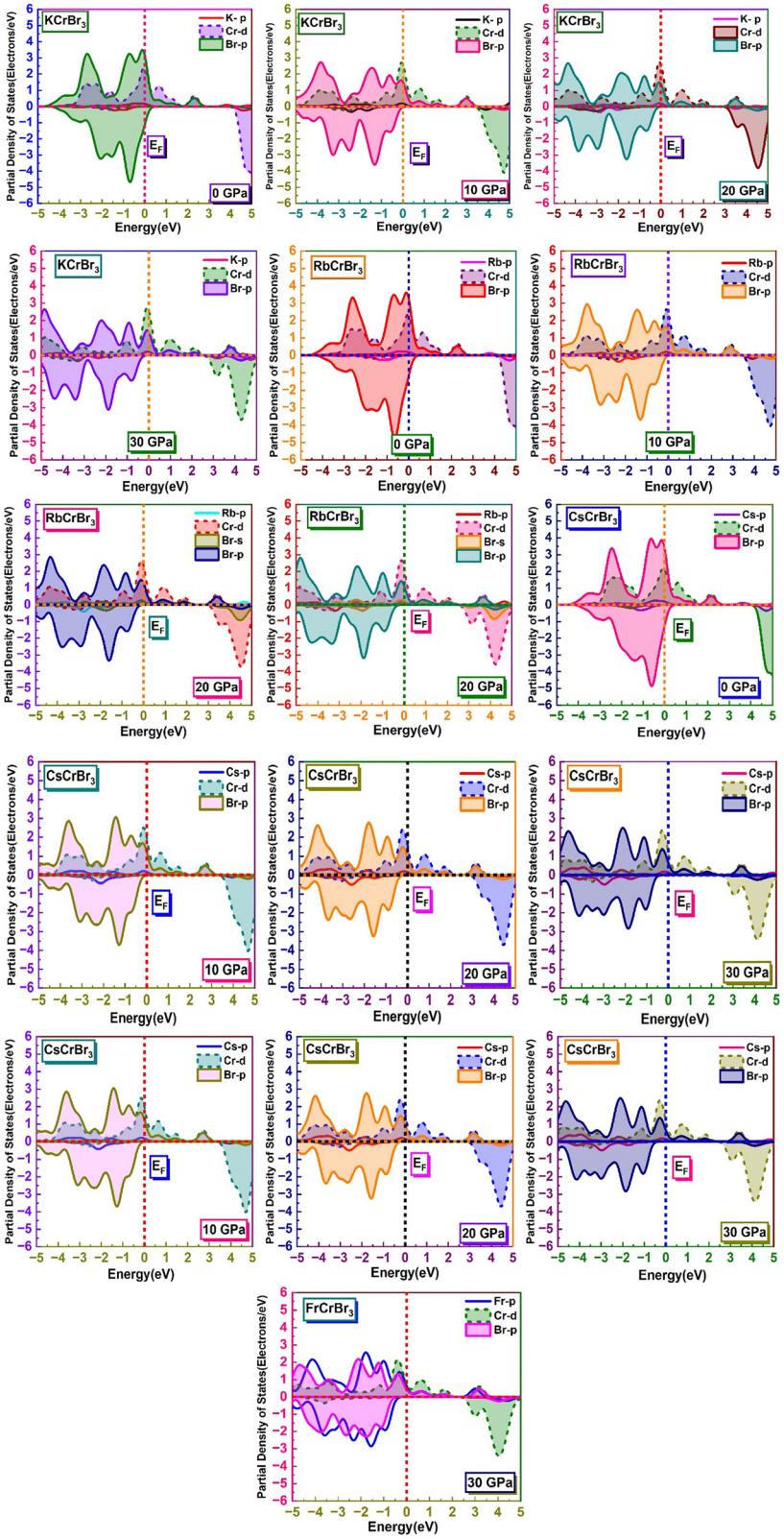

Fig. 10 Calculated spin-polarized partial density of states (PDOS) of $ACrBr_3$ (A = K, Rb, Cs, Fr) perovskites using the GGA+*U* functional.

22.55 eV, 22.78 eV, 24.09 eV, and 24.38, respectively, for K, Rb, Cs, and Fr based materials; it shows a decreasing trend with increasing applied pressure for all investigated systems as seen in Fig. 14(a). As the photon energy increases from 0 eV, the real dielectric response decreases up to approximately 1.05–2.60 eV, after which it rises and displays minor peaks in the ultraviolet

Table 7 Spin magnetic moment (total and atomic) in μ_B of $ACrBr_3$ (A = K, Rb, Cs, Fr) at various pressures using the GGA-PBE and GGA+*U* functionals

		0 GPa		10 GPa		20 GPa		30 GPa	
Magnetic moment	Compounds	GGA	GGA+*U*	GGA	GGA+*U*	GGA	GGA+*U*	GGA	GGA+*U*
Moment-μ_K	$KCrBr_3$	−0.03	0.03, 0.0011[29]	0.04	0.04	0.05	0.04	0.06	0.05
Moment-μ_{Cr}		−3.75	3.93, 3.8341[29]	3.69	3.69	3.41	3.55	3.31	3.44
Moment-μ_{Br}		−0.07	0.02, −0.0383[29]	0.09	0.09	0.18	0.14	0.21	0.17
Total μ		−3.99	4.02, 4[29]	4	4	4	4.01	4	4
Moment-μ_{Rb}	$RbCrBr_3$	0.03	0.03	0.04	0.04	0.05	0.05	0.06	0.06
Moment-μ_{Cr}		3.77	3.94	3.55	3.70	3.42	3.56	3.32	3.45
Moment-μ_{Br}		0.07	0.01	0.13	0.09	0.18	0.13	0.21	0.16
Total μ		4.01	4	3.98	4.01	4.01	4	4.01	3.99
Moment-μ_{Cs}	$CsCrBr_3$	0.03	0.03	0.05	0.05	0.06	0.06	0.08	0.07
Moment-μ_{Cr}		3.79	3.97	3.58	3.73	3.44	3.58	3.34	3.48
Moment-μ_{Br}		0.06	0.00	0.12	0.08	0.16	0.12	0.19	0.15
Total μ		4	4	3.99	4.02	3.98	4	3.99	4
Moment-μ_{Fr}	$FrCrBr_3$	0.03	0.03	0.05	0.04	0.06	0.06	0.07	0.07
Moment-μ_{Cr}		3.81	3.98	3.60	3.75	3.46	3.60	3.36	3.50
Moment-μ_{Br}		0.05	−0.00	0.12	0.07	0.16	0.11	0.19	0.14
Total μ		3.99	4.01	4.01	4	4	3.99	4	3.99

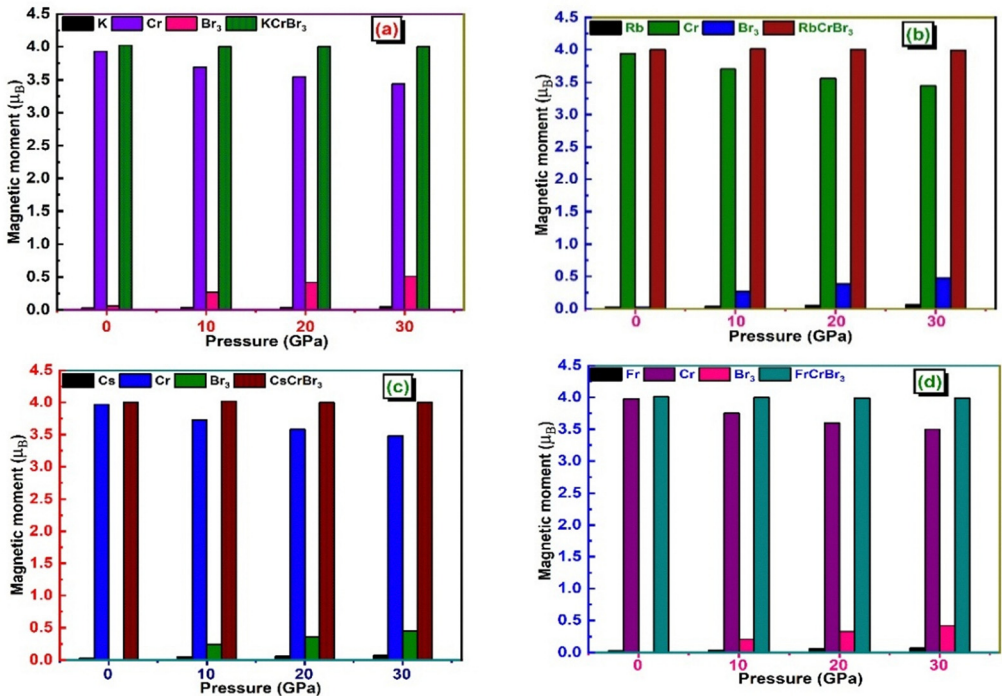

Fig. 11 Magnetic moments in μ_B of (a) $KCrBr_3$, (b) $RbCrBr_3$, (c) $CsCrBr_3$, and (d) $FrCrBr_3$ single perovskites calculated using the GGA+*U* functional.

Table 8 Calculated Curie temperature, T_C (K) at applied pressures 0, 10, 20, and 30 GPa of $ACrBr_3$ (A = K, Rb, Cs, Fr) compounds

	Curie temperature, T_C (K)			
Compounds	0 GPa	10 GPa	20 GPa	30 GPa
$KCrBr_3$	194.78	59.93	423.57	539.55
$RbCrBr_3$	126.43	219.59	407.62	473.98
$CsCrBr_3$	131.28	220.80	384.42	580.33
$FrCrBr_3$	203.63	280.07	340.21	483.38

range. Such a transition from the visible to the ultraviolet spectrum demonstrates the promise of the materials we examined for usage in optoelectronic applications.[62] These peak intensities increase with pressure and also follow a progressive enhancement from K to Fr. Negative values of the real components of the dielectric constants are observed for a certain photon energy range for all of the materials across all pressure ranges. This indicates that our materials behave like a metal at this phonon energy, reflecting incident electromagnetic radiation rather than transmission. The imaginary part of the dielectric function is also presented in Fig. 14(b). The unreal component of the dielectric function $\varepsilon_2(\omega)$ governs a substance's capacity to pass on or collect light. Energy losses in our substances are demonstrated by their peaks and the transition from the valence band maximum to the conduction band minimum, which correspond to interband electronic transitions. With increasing external

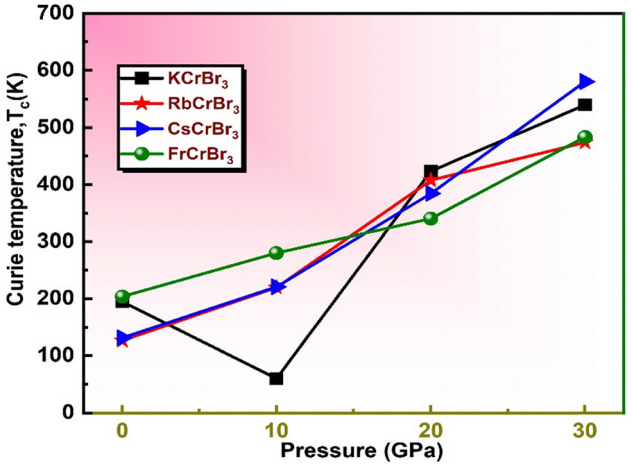

Fig. 12 Variation of the Curie temperature, T_C (K), with applied pressure (GPa) for $ACrBr_3$ (A = K, Rb, Cs, Fr) compounds.

pressure and substitution at the A-site from K to Fr, the magnitude of $\varepsilon_2(\omega)$ also rises. Even though all our studied compounds exhibit a similar qualitative trend the peak values differ. Increasing values of $\varepsilon_2(\omega)$ suggest that the material becomes less transparent, absorbs more light, and provides increased optical loss.[63]

Optical conductivity is the flow of electrons when an electromagnetic wave strikes the material. It additionally provides information on the conduction process. When a material can absorb more photons then it can conduct more electrons, meaning conductivity increases, and both of the graphs show comparable trends. The real part of the optical conductivity under pressure variation is shown in Fig. 14(c) and connected with $\varepsilon_2(\omega)$ by the following relationship:[64]

$$\sigma(\omega) = \frac{\omega}{4}\varepsilon_2(\omega) \quad (30)$$

All four of our investigated compounds show 0 conductivity when the photon energy does not exist. Conductivity for all of our materials is expected to increase with the increase of the photon energy and reach a minor peak, and then it starts to decrease in the infrared (IR) region and becomes minimum in the visible region, as shown in Fig. 14(c). After that, it starts to increase from the visible to the ultraviolet region and shows its highest peak in the UV region. Pressure application increases conductivity, narrowing the band gap of all of our studied materials, which is consistent with our electronic analysis results. The highest conductivity is for the Fr based compound at 30 GPa, whose value is 9.39 (1 fs^{-1}) at 10 eV.

The absorption coefficient can be computed using the following equation,[65]

$$I(\omega) = 2^{\frac{1}{2}}\omega\left[\left\{\varepsilon_1{}^2(\omega) + \varepsilon_2{}^2(\omega)\right\}^{\frac{1}{2}} - \varepsilon_1(\omega)\right]^{\frac{1}{2}} \quad (31)$$

where $\varepsilon_1(\omega)$ and $\varepsilon_2(\omega)$ are the real and imaginary parts of the dielectric function, and the light frequency is represented by ω. This parameter shows a similar trend to the conductivity graph. Under applied pressure, we observe a significant enhancement in the absorption coefficient of all the materials we investigated, and the highest peak is in the UV range, which is 11–18 eV photon energy, which is suitable for the optoelectronic applications.[66]

$$R(\omega) = \left|\frac{\sqrt{\varepsilon(\omega)} - 1}{\sqrt{\varepsilon(\omega)} + 1}\right|^2 \quad (32)$$

Reflectivity, $R(\omega)$, is an optical property and is defined as the ratio of the quantity of light energy falling on a material's surface to the amount of light energy reflected from that surface, and can be calculated from the above equation (eqn (32)). The value of reflectivity without electromagnetic radiation is shown in

Table 9 Effect of pressure on density ρ (kg m^{-3}), Debye temperature θ_D (K), melting temperature T_m (K), Debye frequency ω_D (THz) and minimum thermal conductivity K_{min} (W m^{-1} K^{-1}) of $ACrBr_3$ (A = K, Rb, Cs, Fr) perovskites using the GGA-PBEsol functional

Compounds	Pressure (GPa)	Density, ρ (kg m^{-3})	Longitudinal sound velocity v_l (m s^{-1})	Transverse sound velocity v_t (m s^{-1})	Average sound velocity v_m (m s^{-1})	Debye temperature θ_D (K)	Melting temperature T_m (K)	Debye frequency ω_D (THz)	Minimum thermal conductivity K_{min} (W m^{-1} K^{-1})
$KCrBr_3$	0	3930.17	3750.64	2074.28	2311.05	226.93	919.30	4.73	0.35
	10	4745.74	4898.31	2507.54	2808.96	293.71	1415.33	6.12	0.48
	20	5295.15	5595.74	2751.56	3089.70	335.08	1840.32	6.98	0.56
	30	5719.69	6037.92	2884.20	3243.70	360.94	2207.56	7.52	0.62
$RbCrBr_3$	0	4428.482	3458.28	1939.59	2158.59	211.12	906.36	4.40	0.32
	10	5368.305	4717.09	2453.30	2745.41	286.31	1432.64	5.96	0.46
	20	5962.115	5421.41	2760.70	3093.58	334.10	1854.74	6.96	0.56
	30	6433.694	5893.76	2938.94	3297.46	365.27	2252.66	7.61	0.63
$CsCrBr_3$	0	4863.08	3427.29	1968.79	2186.69	212.11	907.84	4.42	0.32
	10	5878.27	4597.03	2474.04	2762.09	285.40	1410.31	5.94	0.46
	20	6531.10	5310.02	2809.45	3140.34	336.07	1850.90	7.0	0.56
	30	7039.01	5817.30	3031.07	3391.56	372.13	2252.66	7.75	0.63
$FrCrBr_3$	0	5779.795	3157.41	1812.62	2013.34	194.01	899.62	4.04	0.29
	10	7000.131	4248.15	2312.68	2579.77	264.99	1384.89	5.52	0.42
	20	7774.39	4902.24	2613.70	2919.97	310.60	1824.3	6.47	0.51
	30	8378.75	5369.18	2835.38	3169.74	345.69	2218.26	7.20	0.59

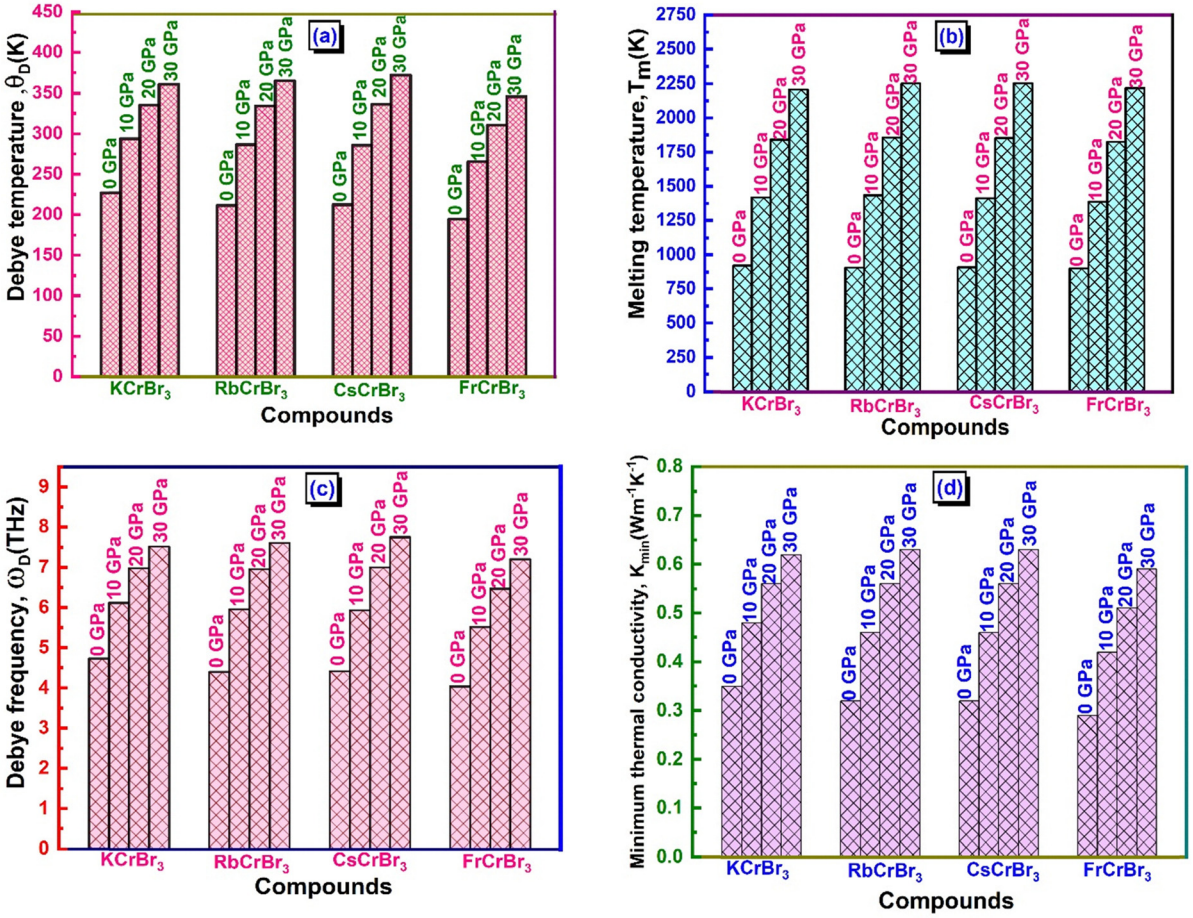

Fig. 13 Variation of (a) Debye temperature θ_D (K), (b) melting temperature T_m (K), (c) Debye frequency ω_D (THz), and (d) minimum thermal conductivity K_{min} (W m^{-1} K^{-1}) with applied pressure 0–30 GPa for $ACrBr_3$ (A = K, Rb, Cs, Fr) compounds.

Fig. 14(e), which almost ranges from 43 to 44% without applied pressure and becomes 31–32% at 30 GPa pressure. Our materials show the highest reflectivity in the UV region, and reflectivity significantly increases with the increase of applied pressure. The Fr based material shows the highest reflectivity, which is 52.6% at 18.62 eV photon energy at 30 GPa pressure.

When light passes through a medium, the amount of light that bounces off from that medium is known as the refractive index. Light can travel quickly within the medium when this value is smaller, and the amount of refraction is less. The refractive index, $\eta(\omega)$, is determined using the following equation:[67]

$$\eta(\omega) = \left[\frac{\sqrt{\varepsilon_1^2(\omega) + \varepsilon_2^2(\omega)}}{2} + \frac{\varepsilon_1(\omega)}{2}\right]^{\frac{1}{2}} \quad (33)$$

All four materials have a high peak at low energy that slowly drops as the energy increases. When pressure is applied, the refractive index becomes a bit higher in the low-energy region. The investigated spectrum is shown in Fig. 14(f). The overall spectral response is almost the same for all our investigated materials.

The loss function $L(\omega)$ as a function of incident photon energy is shown in Fig. 14(g), and this function is the amount of energy an electron loses while traveling through a material. We can compute this using the following formula:[68]

$$L(\omega) = \frac{\varepsilon_2(\omega)}{\varepsilon_1(\omega)^2 + \varepsilon_2(\omega)^2} \quad (34)$$

The highest energy loss occurs in the ultraviolet regions for all of our studied compounds. Pressure has a vital effect on this function, as pressure not only changes the peak value but also shifts the photon energy for which the highest value of the loss function can be found. The highest energy loss for the Cs-based compound is 7.9 at 25 eV photon energy for 30 GPa pressure. The Rb-based material has the highest peak at 20 GPa, and the other two materials also have the highest value at 30 GPa. This peak is generated by bulk plasmonic excitation at a specific incident light energy and the bulk plasma frequency, which is the corresponding frequency at that energy.[69] According to these results, our materials may be promising candidates for spin-polarized optoelectronic devices as well as additional domains[68,70] (Table 10).

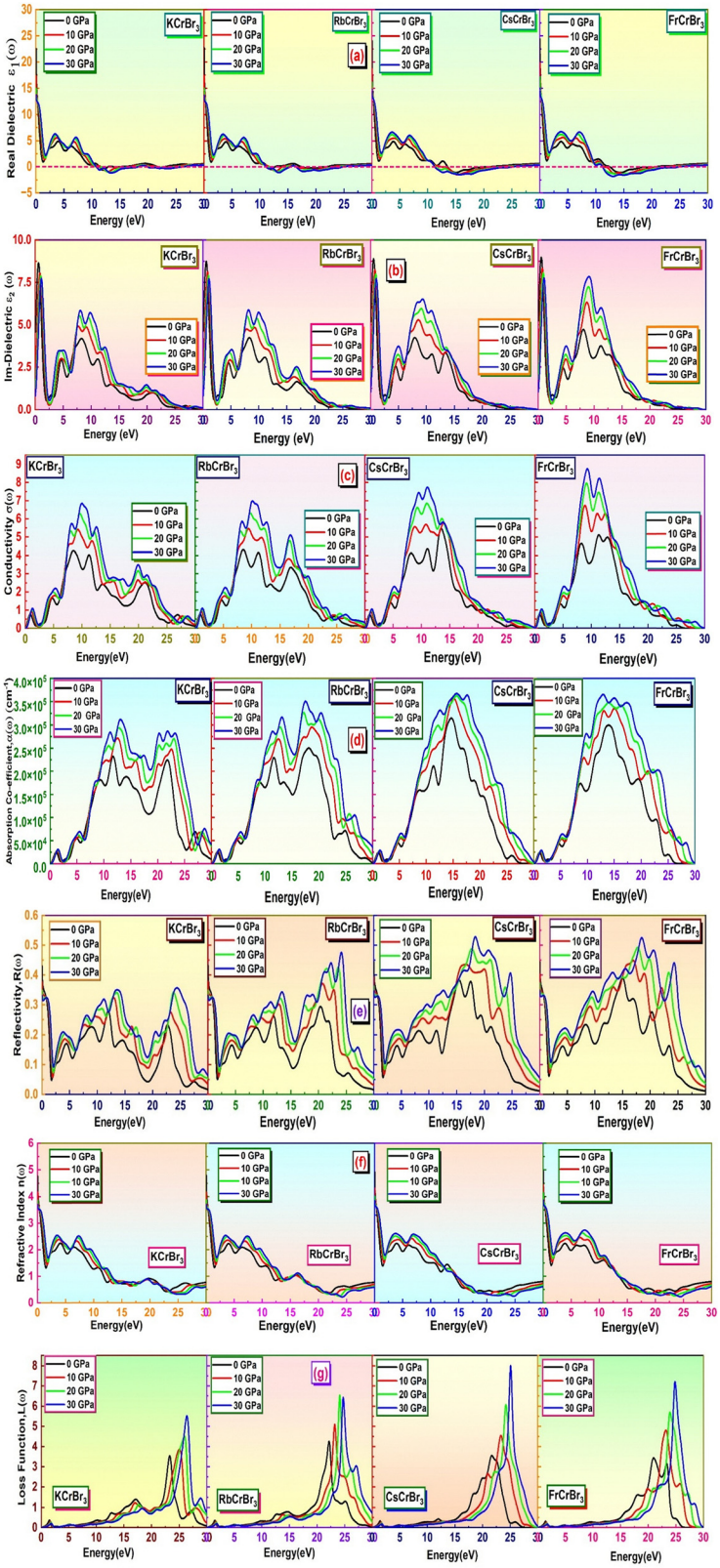

Fig. 14 Photon energy-dependent optical properties: (a) the real part of the dielectric function $\varepsilon_1(\omega)$, (b) the imaginary part of the dielectric function $\varepsilon_2(\omega)$, (c) optical conductivity $\sigma(\omega)$, (d) absorption coefficient $I(\omega)$, (e) reflectivity $R(\omega)$, (f) refractive index, $\eta(\omega)$, and (g) the loss function $L(\omega)$ of $ACrBr_3$ (A = K, Rb, Cs, Fr) compounds at various pressures using the GGA-PBE functional.

Table 10 Static reflectivity, $R(0)$, at various applied pressures for $ACrBr_3$ (A = K, Rb, Cs, Fr)

Compounds	Reflectivity	Pressure (GPa)			
		0	10	20	30
$KCrBr_3$	$R(0)$	0.43	0.38	0.35	0.33
$RbCrBr_3$		0.43	0.38	0.35	0.33
$CsCrBr_3$		0.44	0.39	0.36	0.33
$FrCrBr_3$		0.45	0.40	0.38	0.35

4. Conclusions

In this work, we extensively investigated the structural, mechanical, magnetic, electronic, thermal, and optical properties of cubic $ACrBr_3$ (A = K, Rb, Cs, Fr) perovskites under applied pressures of 0, 10, 20, and 30 GPa using GGA-PBE, GGA+*U*, and GGA-PBEsol functionals. The analysis reveals that Cs- and Fr-based compounds, initially brittle at ambient pressure, transform into ductile materials above 10 GPa, while K- and Rb-based perovskites remain ductile across all studied conditions. Band structure and density of states analyses confirm half-metallicity, and the integer magnetic moment demonstrates stable ferromagnetism. Increasing pressure reduces lattice constants, cell volume, and band gap, while simultaneously enhancing elastic constants, thereby improving rigidity and resilience essential for device integration. Around 10 GPa, the half-metallic gap is maximized for most materials while preserving mechanical stability. Thermodynamic parameters, including Debye temperature and melting temperature, show an upward trend with pressure, indicating enhanced thermal stability. Optical properties are also strongly pressure-dependent, with optical parameters increasing as pressure rises, and the optical conductivity exhibits the largest deviation. Collectively, these findings establish $ACrBr_3$ (A = K, Rb, Cs, Fr) perovskites as robust multifunctional candidates, combining favorable magnetic, mechanical, thermodynamic, and optical characteristics, underscoring their suitability for next-generation spintronic, optoelectronic devices and offering a pathway toward materials capable of showing reliable performance under diverse environmental and operational conditions.

Conflicts of interest

There are no conflicts to declare.

Data availability

The data supporting the findings of this study, including structural parameters, electronic band structures, magnetic properties, elastic properties, and optical properties of $ACrBr_3$ (K, Rb, Cs, Fr), are available from the corresponding author upon reasonable request. No restrictions apply to data sharing.

References

1 S. Das Sarma, Spintronics: a new class of device based on electron spin, rather than on charge, may yield the next generation of microelectronics, *Am. Sci.*, 2001, **89**(6), 516–523, DOI: 10.1511/2001.6.516.
2 M. Y. Sofi, M. S. Khan and M. A. Khan, Spin exchange, electronic correlation, and thermoelectric transport in Rb_2GeMBr_6 (M = V, Mn, Ni) halide double perovskites from first principles calculations, *J. Mater. Chem. C*, 2026, **14**(1), 444–467.
3 S. A. Mir, A. Q. Seh and D. C. Gupta, spintronic applications: $BaMO_3$ ($M\frac{1}{4}$ Mg and Ca), *RSC Adv.*, 2020, **2**, 36241–36252, DOI: 10.1039/d0ra06739c.
4 R. A. De Groot, F. M. Mueller, P. G. Van Engen and K. H. J. Buschow, Half-metallic ferromagnets and their magneto-optical properties, *J. Appl. Phys.*, 1984, **55**(6), 2151–2154.
5 V. A. Online, *RSC Adv.*, 2025, 24002–24018, DOI: 10.1039/d5ra03555d.
6 M. I. Hussain, R. M. A. Khalil, F. Hussain, M. Imran, A. M. Rana and S. Kim, Investigations of structural, electronic and optical properties of $YInO_3$ (Y = Rb, Cs, Fr) perovskite oxides using mBJ approximation for optoelectronic applications: a first principles study, *Mater. Sci. Semicond. Process.*, 2020, **113**, 105064.
7 S. A. Khandy and D. C. Gupta, Structural, elastic and magneto-electronic properties of half-metallic $BaNpO_3$ perovskite, *Mater. Chem. Phys.*, 2017, **198**, 380–385.
8 M. Y. Sofi, M. S. Khan and M. A. Khan, Harnessing the half-metallicity and thermoelectric insights in Cs_2AgMBr_6 (M = V, Mn, Ni) double halide perovskites: a DFT study, *Mater. Sci. Semicond. Process.*, 2025, **186**, 109023.
9 S. A. Khandy and D. C. Gupta, Insight view of double perovskites Ba_2XNbO_6 (X = Ho, Yb) for spintronics and thermoelectric applications, *Int. J. Energy Res.*, 2021, **45**(9), 13338–13354.
10 G. Y. Gao, K. L. Yao, Z. L. Liu, Y. L. Li, J. L. Jiang and Y. C. Li, Half-metallic ferromagnetism of Cr-doped rutile TiO_2: a first-principles pseudopotential study, *Phys. B*, 2006, **382**(1–2), 14–16.
11 Y. Sefir, *et al.*, Structural, electronic, magnetic and thermodynamic properties of the new multifunctional half-Heusler alloy CoTcSn: Half-metallic and ferromagnetic behaviour, *Pramana*, 2021, **95**, 95, DOI: 10.1007/s12043-021-02125-w.
12 L. Beldi, Y. Zaoui, K. O. Obodo, H. Bendaoud and B. Bouhafs, d^0 Half-Metallic Ferromagnetism in GeNaZ (Z = Ca, Sr, and Ba) Ternary Half-Heusler Alloys: an Ab initio Investigation, *J. Supercond. Novel Magn.*, 2020, 3121–3132.
13 S. Omran, Structural stability, electronic structure and magnetic properties of the new hypothetical half-metallic ferromagnetic full-Heusler alloy CoNiMnSi, *Mater. Sci.*, 2016, **34**(1), 85–93.
14 B.-G. Liu, Robust half-metallic ferromagnetism in zinc blende CrSb, *Phys. Rev. B: Condens. Matter Mater. Phys.*, 2003, **67**(17), 172411.
15 A. Rahman, A. Kabir and T. Mahmud, Computational insights into transition metal-based $BaCoX_3$ (X = Cl, Br, I) halide perovskites for spintronics, photovoltaics, and renewable energy devices, *Sci. Rep.*, 2024, **3**, 1–20.
16 J. Berry, *et al.*, Hybrid Organic–Inorganic Perovskites (HOIPs): Opportunities and Challenges, *Adv. Mater.*, 2015, 5102–5112, DOI: 10.1002/adma.201502294.

17 M. A. Green, A. Ho-Baillie and H. J. Snaith, The emergence of perovskite solar cells, *Nat. Photonics*, 2014, **8**(7), 506–514.
18 F. Hao, C. C. Stoumpos, D. H. Cao, R. P. H. Chang and M. G. Kanatzidis, Lead-free solid-state organic–inorganic halide perovskite solar cells, *Nat. Photonics*, 2014, **8**(6), 489–494.
19 S. Kazim, M. K. Nazeeruddin, M. Grätzel and S. Ahmad, Perovskite as light harvester: a game changer in photovoltaics, *Angew. Chem., Int. Ed.*, 2014, **53**(11), 2812–2824.
20 X.-G. Zhao, D. Yang, J.-C. Ren, Y. Sun, Z. Xiao and L. Zhang, Rational design of halide double perovskites for optoelectronic applications, *Joule*, 2018, **2**(9), 1662–1673.
21 K. Mądra-Gackowska, M. Gackowski and Ł. Szeleszczuk, Density Functional Theory Insights into A_2BBiCl_6 (A = Cs, K; B = Ag, Au) Halide Double Perovskites for Next-Generation Photovoltaics, *Phys. B*, 2026, 418286.
22 Ł. Szeleszczuk, K. Mądra-Gackowska, V. B. Hacholli and M. Gackowski, Designing Efficient Energy Materials: Optoelectronic and Thermoelectric Perspectives of X_2YBiCl_6 (X = Cs, Na; Y = Ag, Au) Double Perovskites, *J. Phys. Chem. Solids*, 2025, 113293.
23 Ł. Szeleszczuk, K. Mądra-Gackowska and M. Gackowski, Exploring the Effects of Oxygen Replacement by Sulfur in $SrTiO_3$: A Comprehensive DFT Investigation, *J. Phys. Chem. Solids*, 2026, 113575.
24 D. Ghosh, A. Aziz, J. A. Dawson, A. B. Walker and M. S. Islam, Putting the Squeeze on Lead Iodide Perovskites: Pressure-Induced E ff ects To Tune Their Structural and Optoelectronic Behavior, *Chem. Mater.*, 2019, **31**, 4063–4071, DOI: 10.1021/acs.chemmater.9b00648.
25 A. Ja, Y. Lin, C. M. Beavers, J. Voss, W. L. Mao and H. I. Karunadasa, High-Pressure Single-Crystal Structures of 3D Lead-Halide Hybrid Perovskites and Pressure Effects on their Electronic and Optical Properties, *ACS Cent. Sci.*, 2016, 2–10, DOI: 10.1021/acscentsci.6b00055.
26 V. A. Online, D. Liu, Q. Li, H. Jing and K. Wu, Pressure-induced effects in the inorganic halide, *RSC Adv.*, 2019, 3279–3284, DOI: 10.1039/c8ra10251a.
27 L. Li, Y. Wang, D. Liu, C. Ma, M. G. Brik and A. Suchocki, Comparative fi rst-principles calculations of the electronic, optical, elastic and thermodynamic properties of $XCaF_3$ ($X\frac{1}{4}$ K, Rb, Cs) cubic perovskites, *Mater. Chem. Phys.*, 2017, **188**, 39–48, DOI: 10.1016/j.matchemphys.2016.12.033.
28 C. Li, B. Wang, R. Wang, H. Wang and X. Lu, First-principles study of structural, elastic, electronic, and optical properties of hexagonal $BiAlO_3$, *Phys. B*, 2008, **403**(4), 539–543.
29 H. A. Alburaih and S. Nazir, DFT Calculations of Half-Metallic Ferromagnetism and Transport Properties of Cubic $KCrX_3$ (X = Cl, Br, I) Halides for Spintronics and Energy Conversion Applications DFT Calculations of Half-Metallic Ferromagnetism and Transport Properties of Cubic $KCrX_3$ (X = Cl, Br, I) Halides for Spintronics and Energy Conversion Applications, *J. Electrochem. Soc.*, 2023, **170**(11), 114501, DOI: 10.1149/1945-7111/ad0669.
30 M. U. Khan, A. U. Rahman, M. Ahmad, M. Yaseen and M. A. Ahmed, Exploring room-temperature ferromagnetism and half-metallicity in new halide perovskites $RbCrX_3$ (X: F, Cl, Br, I) using first-principles and Monte Carlo simulations, *Eur. Phys. J. Plus*, 2024, **139**, 106, DOI: 10.1140/epjp/s13360-024-04898-6.
31 P. J. D. Lindan, *et al.*, First-principles simulation: ideas, illustrations and the CASTEP code, *J. Phys.: Condens. Matter*, 2002, **14**(11), 2717–2744.
32 M. Karouchi, *et al.*, Investigating the structural, electronic, and optical properties of the novel double perovskite K_2AgBiI_6 using DFT, *Front. Mater.*, 2024, **11**, 1–11, DOI: 10.3389/fmats.2024.1448400.
33 T. H. Fischer and J. Almlof, General methods for geometry and wave function optimization, *J. Phys. Chem.*, 1992, **96**(24), 9768–9774.
34 J. P. Perdew, K. Burke and M. Ernzerhof, Generalized gradient approximation made simple, *Phys. Rev. Lett.*, 1996, 77(18), 3865.
35 M. Y. Sofi, M. S. Khan and M. A. Khan, Eco-friendly lead-free halide double perovskites A_2CuMCl_6 (A = K, Rb; M = Sb, Bi): stability, thermoelectric, and optoelectronic advancements through theoretical insights, *J. Mater. Chem. C*, 2024, **12**(39), 16045–16058.
36 R. Hossain, S. Khanom and P. Mondal, Materials Advances (Pb): a comparative first-principles study for multifunctional device applications, *Mater. Adv.*, 2026, 618–640, DOI: 10.1039/d5ma00961h.
37 M. Y. Sofi, M. S. Khan and M. A. Khan, Materials Advances candidates for semiconductor spintronics and, *Mater. Adv.*, 2024, 4913–4931, DOI: 10.1039/d3ma01160g.
38 M. K. Shahzad, *et al.*, Computational investigation on physical properties of lead based perovskite $RPbBr_3$ (R = Cs, Hg, and Ga) materials for photovoltaic applications, *Sci. Rep.*, 2024, 1–13, DOI: 10.1038/s41598-024-70586-1.
39 Ł. Szeleszczuk, K. Mądra-Gackowska and M. Gackowski, Optoelectronic and Thermoelectric Performance of Cubic X_2YInO_6 (X = Ba, Sr; Y = Nb, V) Double Perovskites: A First-Principles Approach, *Phys. B*, 2025, 417958.
40 K. A. Persson, Lattice instabilities in metallic elements, *Rev. Mod. Phys.*, 2012, **84**, 945–986, DOI: 10.1103/RevModPhys.84.945.
41 M. A. Haq, Ultra-violet to visible band gap engineering of cubic halide $KCaCl_3$ perovskite under pressure for optoelectronic applications: insights from DFT, *RSC Adv.*, 2021, 36367–36378, DOI: 10.1039/D1RA06430D.
42 J. Gao, Q.-J. Liu and B. Tang, Elastic stability criteria of seven crystal systems and their application under pressure: taking carbon as an example, *J. Appl. Phys.*, 2023, **133**(13), 135901.
43 A. Bakar, A. O. Alrashdi, M. M. Fadhali, A. Afaq, H. A. Yakout and M. Asif, Effect of pressure on structural, elastic and mechanical properties of cubic perovskites $XCoO_3$ ($X\frac{1}{4}$ Nd, Pr) from first-principles investigations, *J. Mater. Res. Technol.*, 2022, **19**, 4233–4241, DOI: 10.1016/j.jmrt.2022.06.126.
44 N. Hasan, Structural, elastic and optoelectronic properties of, *RSC Adv.*, 2022, 7961–7972, DOI: 10.1039/d2ra00546h.
45 R. Hill, The elastic behaviour of a crystalline aggregate, *Proc. Phys. Soc., London, Sect. A*, 1952, **65**(5), 349.

46 M. Faghihnasiri, M. Izadifard and M. E. Ghazi, DFT study of mechanical properties and stability of cubic methylammonium lead halide perovskites ($CH_3NH_3PbX_3$, X = I, Br, Cl), *J. Phys. Chem. C*, 2017, **121**(48), 27059–27070.

47 S. I. Ranganathan and M. Ostoja-starzewski, Universal Elastic Anisotropy Index, *Phys. Rev. Lett.*, 2008, **055504**, 3–6, DOI: 10.1103/PhysRevLett.101.055504.

48 A. Hosen, R. Islam and S. Haque, Heliyon Exploring the influence of pressure-induced semiconductor-to-metal transition on the physical properties of cubic perovskites FrXCl 3 (X = Ge and Sn), *Heliyon*, 2024, **10**(7), e27581, DOI: 10.1016/j.heliyon.2024.e27581.

49 M. H. Miah, *et al.*, First-principles study of the structural, mechanical, electronic, optical, and elastic properties of non-toxic $XGeBr_3$ (X = K, Rb, and Cs) perovskite for optoelectronic and radiation sensing applications, *Mater. Chem. Phys.*, 2024, **319**, 129377.

50 S. Muramatsu and M. Kitamura, Simple expressions for elastic constants C_{11}, C_{12}, and C_{44} and internal displacements of semiconductors, *J. Appl. Phys.*, 1993, **73**(9), 4270–4272.

51 M. I. Naher and S. H. Naqib, An *ab initio* study on structural, elastic, electronic, bonding, thermal, and optical properties of topological Weyl semimetal TaX (X = P, As), *Sci. Rep.*, 2021, 1–21, DOI: 10.1038/s41598-021-85074-z.

52 A. Ganguly, V. Murthy and K. Kannoorpatti, Structural and electronic properties of chromium carbides and Fe-substituted chromium carbides Structural and electronic properties of chromium carbides and Fe-substituted chromium carbides, *Mater. Res. Express*, 2020, **7**(5), 056508.

53 L. B. M. Taibi and A. B. M. Abd, Dielectric relaxation, electrical conductivity and optical studies of solid – state synthesized – $EuCrO_3$, *J. Mater. Sci.: Mater. Electron.*, 2020, **31**(1), 354–360, DOI: 10.1007/s10854-019-02533-0.

54 K. S. R. Kumar, Half-metallic behavior of Co_2YZ (Y_5V, Cr; Z_5Al, Ga) under pressure: a DFT study, *Appl. Phys. A*, 2014, 1199–1209, DOI: 10.1007/s00339-013-8211-4.

55 G. Y. Gao, L. Hu, K. L. Yao, B. Luo and N. Liu, Large half-metallic gaps in the quaternary Heusler alloys CoFeCrZ (Z = Al, Si, Ga, Ge): a first-principles study, *J. Alloys Compd.*, 2013, **551**, 539–543.

56 S. A. Mir and D. C. Gupta, New ferromagnetic half-metallic perovskites for spintronic applications: $BaMO_3$ (M = Mg and Ca), *RSC Adv.*, 2020, **10**(60), 36241–36252.

57 M. Y. Sofi, *et al.*, Pioneering computational insights into the structural, magnetic, and thermoelectric properties of A_3XN (A = Co, Fe; X = Cu, Zn) anti-perovskites for advanced material applications, *Mater. Sci. Semicond. Process.*, 2025, **185**, 108925.

58 V. N. Jafarova, First-Principles Study of the Effects of Dopant Concentration on the Electronic, Magnetic, and Structural Properties of Mn-Doped ZnO, *J. Supercond. Novel Magn.*, 2026, **39**, 31.

59 P. Ravindran, L. Fast, P. A. Korzhavyi, B. Johansson, J. Wills and O. Eriksson, Density functional theory for calculation of elastic properties of orthorhombic crystals: Application to $TiSi_2$, *J. Appl. Phys.*, 1998, **84**(9), 4891–4904.

60 M. A. Rehman, J. ur Rehman and M. B. Tahir, Density functional theory study of structural, electronic, optical, mechanical, and thermodynamic properties of halide double perovskites $Cs_2AgBiX6$ (X = Cl, Br, I) for photovoltaic applications, *J. Phys. Chem. Solids*, 2023, **181**, 111443.

61 N. Shahadath and R. Kabir, OPEN DFT analysis of structural, electronic, optical, and thermodynamic properties of $LiXI_3$ (where X = Ca, Sr, Ba) halide perovskites for optoelectronics, *Sci. Rep.*, 2025, 1–23.

62 S. M. Ramay, Study of pressure induced physical properties of $ZnZrO_3$ perovskite using density functional theory, *Chem. Phys. Lett.*, 2020, 137601, DOI: 10.1016/j.cplett.2020.137601.

63 Y. Didi, *et al.*, Computational insights into spin-polarized density functional theory applied to actinide-based perovskites $XBkO_3$ (X = Sr, Ra, Pb), *Sci. Rep.*, 2025, 1–15.

64 J. M. Khoshman, P. Jakkala, D. C. Ingram and M. E. Kordesch, Optical conductivity tuning and electrical properties of a-Be_xZn_yO thin films, *J. Non.-Cryst. Solids*, 2016, **440**, 31–37.

65 X. Cr, M. M. Parvaiz, A. Khalil and B. Tahir, magnetic, optical, elastic and hydrogen storage, *RSC Adv.*, 2024, 8385–8396, DOI: 10.1039/d4ra00204k.

66 M. K. Butt and M. Yaseen, First Principle Insight into the Structural, Optoelectronic, Half Metallic, and Mechanical Properties of Cubic Perovskite $NdInO_3$, *Arabian J. Sci. Eng.*, 2020, 4967–4974.

67 A. Ramzan, M. Y. Sofi, M. S. Khan, J. Ali and M. A. Khan, Regular Article – Computational Methods First-principles investigation of Mg-based $MgAl_2X_4$ (X = S, Se) spinels for optoelectronic and energy harvesting, *Eur. Phys. J. B*, 2025, **98**(5), 1–11, DOI: 10.1140/epjb/s10051-025-00937-y.

68 R. Hossain, S. Khanom, P. Mondal and F. Ahmed, Signature of half-metallicity and pressure-induced physical properties of Cubic $ACrO_3$ (A = Si,Ge,Sn) multiferroic by DFT calculation, *Mater. Adv.*, 2025, **6**, 6550–6566, DOI: 10.1039/d5ma00169b.

69 A. Hossain, M. S. I. Sarker, M. K. R. Khan and M. M. Rahman, Spin effect on electronic, magnetic and optical properties of spinel $CoFe_2O_4$: A DFT study, *Mater. Sci. Eng., B*, 2020, **253**, 114496, DOI: 10.1016/j.mseb.2020.114496.

70 A. Javed, Q. Ain, A. Kumar, L. El, A. Kais and O. S. E. Shcheklein, Spin-Polarized DFT Based Investigation of $Cs_2LiMoBr_6$: A Promising Candidate for Spintronics, Optoelectronics and Sustainable Energy Systems, *J. Supercond. Novel Magn.*, 2026, 1–12.